ELSEVIER

Contents lists available at ScienceDirect

## Remote Sensing of Environment

journal homepage: www.elsevier.com/locate/rse



# Does intensity-based weighting of multiple-return terrestrial LiDAR data improve leaf area density estimates?

Eric R. Kent\*, Brian N. Bailey

Department of Plant Sciences, University of California, Davis, USA

### ARTICLE INFO

Edited by Jing M. Chen

Keywords: Canopy structure Multi-return LiDAR Leaf area density Terrestrial laser scanning

### ABSTRACT

Terrestrial LiDAR scanning (TLS) data can be used to efficiently estimate plant canopy structural variables including leaf area density (LAD). This is done by estimating the transmission probability of LiDAR beams through a canopy, which is directly related to the local LAD. Advancements in TLS technology have enabled instruments that can record multiple object intersection points along a single laser pulse path, but whether this additional information can improve LAD estimation from TLS is not fully understood. Several methods for incorporating multiple returns per beam into transmission probability and LAD estimations have been previously suggested, including the use of corrected relative intensity to weight multiple returns more precisely. Intensity-based weighting is complicated by unknown variation in surface reflectance and orientation.

Synthetic multiple-return TLS simulations were performed for virtual homogeneous voxels and heterogeneous tree cases with known properties (LAD, leaf angle distribution, reflectivity) in order to evaluate LAD estimates using intensity-based weighting in comparison to first-hits and equal-weighting approaches. An idealized intensity-based weighting, where the fraction of beam energy hitting every surface is known, and an exact weighting, where the impact of partial misses is also accounted for were also analyzed.

Intensity-based weighting of multiple-return TLS data did not necessarily improve transmission probability and LAD estimates compared with the more simple equal-weighting method. Both methods had relatively similar performance, with the intensity-weighting method tending towards slightly lower transmission and higher LAD. There could be significant errors for all methods, including when weighting of hit points was exact. The error in LAD caused by choice of weighting method was therefore sometimes overshadowed by a combination of other errors due to clumping, partial misses, voxel occlusion, and limitations of Beer's law for dense canopies, which could have substantial impacts. Given the small, but inconsistent potential improvements in accuracy of the intensity-based methods that were tested in this work, the equal-weighting method appears an acceptable choice.

## 1. Introduction

Remotely-sensed data describing plant canopy structure are used to provide inputs for a spectrum of models ranging from large-scale weather and climate models (e.g., Lu and Shuttleworth, 2002; Yuan et al., 2011) to detailed 3D leaf-resolving functional-structural plant models (e.g., Sievänen et al., 2018; Bailey, 2019; Perez et al., 2022). Manual measurements of canopy structure are usually time consuming, sometimes destructive, and infeasible for most applications involving scales larger than that of individual plants. Remote sensing, including laser scanning (LS) has become an increasingly prevalent means for rapidly quantifying vegetation structure. While passive remote sensing platforms have been used for many decades to measure two-dimensional (2D) variation in vegetation structure, active sensing approaches such as airborne and terrestrial laser scanning (ALS and

TLS, respectively) have been more recently used to quantify two- or three-dimensional (3D) variation in canopy gap fraction (e.g., Danson et al., 2007; Ramirez et al., 2013), leaf angle distributions (e.g., Bailey and Mahaffee, 2017a; Itakura and Hosoi, 2019), and leaf area (e.g., Riano et al., 2004; Hosoi and Omasa, 2006; Jupp et al., 2009; Béland et al., 2011; Halubok et al., 2022), among other parameters. Using TLS to estimate LAD, defined here as the one-sided leaf area per unit volume (i.e., leaf area density), is the focus of the present article.

The typical approach for extracting LAD information from raw LiDAR data is to divide a plant or canopy into discrete 3D volumes called voxels. Intersection of the laser pulses (also referred to as 'beams' in this work) emitted by the scanner with plant matter inside the voxels is used to statistically estimate the density of leaves (or plant surfaces in general) within each voxel. Previous work has done so using a point

E-mail addresses: erkent@ucdavis.edu (E.R. Kent), bnbailey@ucdavis.edu (B.N. Bailey).

Corresponding author.

quadrant analogy (e.g., Radtke and Bolstad, 2001; Hosoi and Omasa, 2006; Béland et al., 2014; Bailey and Mahaffee, 2017b) or inversion of Beer's Law (e.g., Bailey and Mahaffee, 2017b; Pimont et al., 2018) to estimate LAD within voxels. Much previous work has only considered a single aggregated return per laser pulse (e.g., Pimont et al., 2015; Bailey and Mahaffee, 2017b; Soma et al., 2018). Current generation scanners typically have the capability of recording multiple returns (also referred to as 'hits', 'hit points', and 'echos' in this work) along a single beam when the beam cross-section partially intersects multiple surfaces along its path. This extra information pertaining to multiple hits per laser pulse could potentially improve LAD estimates, but how to best incorporate it into current processing of LS data is an active area of research.

Previous studies explored a simple method in which multiple simulated LS returns in a single beam are weighted equally and each beam is weighted equally (e.g., Armston et al., 2013; Grau et al., 2017). This method is easy to apply because only the number of returns in each laser pulse is needed, which is typically recorded by the LS instrument for each data point. Other work has used intensity values associated with individual returns in their weighting schemes to calculate canopy gap fraction and/or LAD with ALS data (e.g., Hopkinson and Chasmer, 2007; Armston et al., 2013; Heiskanen et al., 2015; Hancock et al., 2017, 2019) or TLS data (e.g., Hancock et al., 2015b, 2017). In these type of approaches, for example, a weak return resulting from the beam barely glancing the edge of a leaf would be weighted much less than a strong return resulting from most of a beam being intercepted by another leaf. In practice, corrected intensity-based weighting is difficult because it requires knowledge of other factors affecting return intensity such as the distances, angles and reflectivities of the different objects generating the returns, as well as information about the methods used by instruments to convert full-waveform data into returns, which is often proprietary.

Yin et al. (2020) recently conducted a comparison of several methods, including equal-weighting and intensity-based methods for simulations of ALS data, but comparisons of different multi-return weighting methods have not been previously explored for LAD estimation with TLS data. TLS and ALS data differ in several respects including the cross-sectional or "footprint" area of the laser beams, the typical size of the voxels, the scan density, and the positioning of the scanner relative to the voxels. In the case of ALS, the scanner is always above the voxels and any beams transmitted through all voxels encounter the ground. In the case of TLS data, the scanner can be below, at the level of, or above any given voxel. When measuring taller vegetation such as orchards or forests, the scanner is typically below most of the voxels of interest. Beams transmitted through any given voxel may encounter other vegetation or surfaces, or may not encounter any surfaces (i.e., misses). Based on the specified scan pattern or by using gap-filling, beams that are not associated with any echoes can be accounted for in estimations of LAD. Beams that only partially miss, however, remain unaccounted for, and this causes an underestimation of transmittance through the voxel and an overestimation of LAD (Grau et al., 2017).

The goal of this study was to evaluate several methods of incorporating multiple return information into LAD estimates using TLS data. Of particular interest were potential improvements of intensity-based weighting methods over equal-weighting methods, as well as the impact of partial misses. Simulations were used to investigate the methods for homogeneous voxels and heterogeneous trees in which canopy geometry and the exact fraction of beam energy hitting each surface in a scene (or not hitting any surface) were known.

## 2. Materials and methods

## 2.1. Simulated multi-return TLS

Simulations provide an invaluable tool for investigating and evaluating TLS data processing methods since parameters that are fixed

or unknown in real-world situations can be systematically varied. This work adapts GPU ray-tracing-based discrete TLS scanning simulations used by Bailey and Mahaffee (2017b) and Bailey and Ochoa (2018) to incorporate the additional information provided by multiple-return TLS. The multiple-return synthetic TLS data generation and data processing methods presented herein were implemented as a plug-in for the Helios modeling framework (Bailey, 2019). As in previous single-return simulations, the locations of the scan(s), the range of azimuthal ( $\phi$ ) and zenithal ( $\theta$ ) angles over which to scan, the number of beams to send out in each direction, and the location, size, and subdivisions of the voxels for which LAD is to be calculated are provided by the user. In the multiple-return version, the user also specifies the effective beam diameter at exit, beam divergence angle, the number of rays used to represent a single beam, and a bin size ( $B_s$ ) over which rays are aggregated for the purpose of peak detection.

The user-specified number of rays is sent out for each beam (i.e.,  $\phi$  and  $\theta$  combination) according to the specified scan pattern. 500 rays per beam were used in this study, following Grau et al. (2017). The rays are sent out from locations on the beam cross-section randomly sampled from a Gaussian distribution. The distribution is defined such that the probability a ray is launched at the user-specified beam diameter is  $1/e^2$  of the probability at the beam center. Each ray is sent out at the beam  $\phi$  and  $\theta$  angle with a random perturbation between zero and the user-defined beam divergence.

The geometry being scanned (e.g., leaves and branches) is represented by a polygon mesh (rectangles or triangles) and ray-polygon intersection tests are performed for each ray to determine the hit location. All the rays in a given beam are ordered by the distance at which they intersected an object. Individual rays are binned from zero to the maximum scanner range into bins of  $B_s$  width (set to 1 cm in this study). The scanner range was set to 1000 m for simulations in this study, which is in the range of maximum measurement ranges reported for the RIEGL VZ-1000 scanner (RIEGL Laser Measurement Systems GmbH; Horn, Austria). The sum of intensities is calculated for all rays within each bin. A peak detection algorithm is used to find peaks in intensity and a hit point is created at each peak. The minimum bin intensity between adjacent peaks was used as a break point to determine which bins belonged to which peaks. The intensity of the hit point was then determined by the sum of the intensities for the relevant group of bins. This method could result in hit points in close proximity to each other, unlike for actual TLS data where there is a multi-target resolution, a minimum distance between two hit points within one beam. This minimum distance is specified as a pulse distance threshold parameter,  $T_{pd}$ . Hit points within  $T_{pd}$  of each other were merged into single hit points. Merging began with the nearest hit point to the scanner and any other hit points within  $T_{pd}$  were merged into a single point with a distance from the scanner determined by the intensity-weighted distance of the constituent hit points. This process continued with the next closest hit point that was not already merged.  $T_{nd}$  was set to 11 cm based on the smallest distance between echoes within the same beam observed in TLS datasets acquired with a RIEGL VZ-1000 scanner in an almond orchard. The approach employed here is similar to, but may be more simplified than, approaches used by actual TLS scanners, which are usually based on proprietary Gaussian fitting techniques in order to extract echoes from TLS waveform data. The simulations used in this work also do not attempt to accurately represent instrument system specifics related to sensor triggering, signal-to-noise levels, and deadtime, which can impact estimated vegetation parameters with actual sensors (e.g., Disney et al., 2010; Hancock et al., 2015a; Anderson et al., 2016; Hancock et al., 2019). These instrument system properties/limitations may introduce additional uncertainties compared to the simplified/idealized simulations performed in this study.

In this work, three different combinations of beam diameter and beam divergence values were tested. The reference case consisted of a 7 mm exit diameter beam with divergence of 0.3 mrad, corresponding to the values for the RIEGL VZ-1000 TLS scanner. A smaller beam with

one half the diameter and divergence of the reference case, as well as a larger beam with double the diameter and divergence of the reference case were also tested. Scan resolutions were  $0.06^{\circ}$  and  $0.0667^{\circ}$  in the azimuthal and zenithal directions, respectively.

## 2.2. Estimation of leaf area density from TLS data

Inversion of the Beer–Lambert Law to estimate leaf area density within a voxel is the preferred method for LAD estimation used in recent TLS work (e.g., Bailey and Mahaffee, 2017b; Grau et al., 2017; Bailey and Ochoa, 2018) and is adopted here. The Beer–Lambert Law describes the probability of radiation interception by a participating medium, and can be written in the context of a laser pulse traveling through vegetation as (Bailey and Mahaffee, 2017b):

$$\overline{P} = \frac{1}{B_{tot}} \sum_{k=1}^{B_{tot}} \exp(-LAD \cdot \overline{G} \cdot r_k), \tag{1}$$

where  $\overline{P}$  is the average probability of a beam passing through a voxel without intersecting a leaf,  $B_{tot}$  is the number of beams entering the voxel, LAD is the one-sided leaf area per unit volume (i.e., leaf area density) in the voxel,  $\overline{G}$  is the voxel average fraction of projected leaf area in the direction of beam propagation, and  $r_k$  is the kth beam path length through the entire voxel (irrespective of whether there was a hit inside the voxel). This equation is an aggregation of Beer's law over multiple beams and is based on the assumption of homogeneous vegetation within the voxel.

Eq. (1) is solved iteratively for LAD since an explicit analytical solution is not possible given its functional form. In instances where the iterative solution does not converge or converges to an unrealistic value, a simplified method with an algebraic solution which uses the mean value of  $r_k$  instead of performing the calculation for each beam can be used. Bailey and Mahaffee (2017b) showed that the simplified analytical solution using average ray path length always underestimates the iterative form, and Grau et al. (2017) provide an approximate expression for the magnitude of error involved. In the present study, the impact of using the analytical solution to gap-fill the iterative one had a negligible impact on estimated leaf area. The analytical solution was required for only a small fraction (less than 5%) of LAD calculations and was predicted to underestimate the total leaf area with the iterative solution for these cases by a fraction of a percent.  $\overline{G}$  may be estimated from TLS data using triangulation of hit points (Bailey and Mahaffee, 2017a), or is assumed to follow some known distribution (e.g., uniform or spherical). To isolate the impact of different methods for estimating  $\overline{P}$  on LAD, this work used the exact value of  $\overline{G}$  known for each virtual canopy from the geometric model,  $\overline{G}_{ref}$ . In actual TLS measurements of real-world canopies, estimating  $\overline{G}$  would create additional uncertainty in the estimation of LAD.  $r_k$  was calculated based on the beam direction and the locations of the scanner and the voxel.

A reference value of transmission probability,  $\overline{P}_{ref}$ , was calculated using Eq. (1) and the known values of leaf area density  $(LAD_{ref})$  and  $\overline{G}_{ref}$  for each canopy. Comparisons were made against  $\overline{P}_{ref}$  to evaluate the other methods for estimating  $\overline{P}$  tested in this work, which had the same functional form:

$$\overline{P}_{x} = \frac{\sum_{k=1}^{B_{tot}} T_{k}^{x} \cdot BW_{k}^{x}}{\sum_{k=1}^{B_{tot}} BW_{k}^{x}},$$
(2)

where x denotes a label for a given method,  $T_k$  is the transmission estimated from the kth beam, and  $BW_k$  is a beam weighting term that may incorporate one or more factors as discussed below. In the equations for each individual method (Eqs. (6), (8), (11), (9), and (12)) the transmission term is written out, but the beam weighting term is not expanded for brevity. Table 1 provides a summary of all terms for each method tested in this work.

Table

Methods of estimating transmission probability tested, and definitions of transmission and beam weighting terms in Eq. (2).  $w_k$  is 1 if the first echo of the kth LiDAR beam hit something after the voxel and zero otherwise.  $E_k^{after}$  and  $E_k^{inside}$  are the number of echoes (hit points) after the voxel and inside the voxel associated with the kth beam, respectively.  $I_{after}^k$  and  $I_{inside}^k$  are the simulated intensities of the echoes from after the voxel and inside the voxel for the kth beam, respectively.  $R_k^{after}$  and  $R_k^{inside}$  are the number of simulated rays in the kth beam that intersect objects after the voxel and inside the voxel, respectively.

P method	Transmission term $(T_k)$	Beam weighting term $(BW_k)$
$\overline{P}_{first}$ first-hits	$w_k$	1
$\overline{P}_{equal}$ equal-weighting	$\frac{E_k^{after}}{E_k^{inside} + E_k^{after}}$	$\frac{E_k^{inside} + E_k^{after}}{E_k^{before} + E_k^{inside} + E_k^{after}}$
$\overline{P}_{intensity}$ intensity-weighting	$\frac{I_k^{after}}{I_k^{inside} + I_k^{after}}$	$\frac{I_k^{inside} + I_k^{after}}{I_k^{before} + I_k^{inside} + I_k^{after}}$
$\overline{P}_{ideal}$ ideal intensity-weighting	$\frac{R_k^{after}}{R_k^{inside} + R_k^{after}}$	$\frac{R_k^{inside} + R_k^{after}}{R_k^{before} + R_k^{inside} + R_k^{after}}$
$\overline{P}_{exact}$ exact-weighting	$\frac{R_k^{after} + R_k^{miss}}{R_k^{inside} + R_k^{after} + R_k^{miss}}$	$\frac{R_k^{inside} + R_k^{after} + R_k^{miss}}{R_k^{before} + R_k^{inside} + R_k^{after} + R_k^{miss}}$

Beam weighting terms for all methods originally contained a term to weight by the sine of the beam zenith angle based on the idea that there was a greater density of beams at lower zenith angles for spherical scan patterns typically employed with TLS (Bailey and Mahaffee, 2017b). Questions from one anonymous reviewer led to our retesting of this term. While the term had little impact on estimated transmission probability with the scan configurations typical of TLS, it had non-negligible impact for extreme cases where the scanner was positioned very close to relatively large voxels (not shown). In these cases, more accurate transmission probability was estimated without the sine weighting term. Consequently, the term was removed from the calculations reported in this article.

For the purposes of quantifying agreement between reference values (i.e.,  $\overline{P}_{ref}$  and  $LAD_{ref}$ ) and estimates calculated with the different weighting methods, three statistics also employed by Bailey and Mahaffee (2017b) were used. Mean bias was calculated as:

$$bias = \frac{1}{N} \sum_{i=1}^{N} (x_i - ref_i), \tag{3}$$

index of agreement was calculated as:

$$d = 1 - \frac{\sum_{i=1}^{N} (ref_i - x_i)^2}{\sum_{i=1}^{N} (|ref_i - \overline{ref}| + |x_i - \overline{ref}|)^2},$$
(4)

and normalized root-mean-squared error (nRMSE) was calculated as:

$$nRMSE = \frac{\sqrt{\frac{1}{N} \sum_{i=1}^{N} (ref_i - x_i)^2}}{\overline{ref}},$$
 (5)

where N is the number of voxels,  $x_i$  is the value of  $\overline{P}$  or LAD estimated for the ith voxel, and  $ref_i$  is  $\overline{P}_{ref}$  or  $LAD_{ref}$  for the ith voxel.  $\overline{ref}$  is the mean value of  $\overline{P}_{ref}$  or  $LAD_{ref}$  over all voxels in the calculation. nRMSE is expressed here and in the figures as a fraction, but is also expressed as a percentage in text by multiplying by 100.

## 2.3. First-hits method

The first-hits method is based on applying single-return methods to the first echo (hit point) of each beam of multi-return TLS data, essentially ignoring everything but the first echo. Using single-return TLS data, Bailey and Mahaffee (2017b) estimated  $\overline{P}$  as follows:

$$\overline{P}_{first} = \frac{\sum_{j=1}^{B_{after}} BW_j^{first}}{\sum_{k=1}^{B_{tot}} BW_k^{first}} = \frac{\sum_{k=1}^{B_{tot}} w_k \cdot BW_k^{first}}{\sum_{k=1}^{B_{tot}} BW_k^{first}},$$
(6)

where the sequence  $j=1...B_{after}$  corresponds to beams that traversed the entire voxel without intersecting an object, the sequence  $k=1...B_{total}$  represents all beams that entered the voxel,  $w_k$  is 1 if the beam (or first beam echo in the case of multiple-return TLS) first hit something after the voxel (i.e., was transmitted through the voxel) and zero otherwise.

The implicit assumption of Eq. (6) is that beams are infinitely small in diameter so that they are either associated with a single echo (hit point), or produce no echo (misses). Some TLS instruments do not record information about beams that produce a very weak echo (i.e., there is no corresponding hit point), but these beams still need to be considered in the calculation of  $B_{tot}$ . They can be estimated from the locations of the scanner and voxel as well as the scan resolution in the zenithal and azimuthal directions (e.g., Grau et al., 2017), or they can be estimated by gap-filling the hit point data set. The latter approach may theoretically be more accurate than a simplified calculation based on scan resolution since it can account for the influence of scanner tilt and azimuthal movement of the scanner as the full range in the zenithal directions is sampled.

In reality, beams are of a small, but finite diameter and can partially hit multiple objects before, inside, or after traversing a voxel, and a portion of the beam can also produce no hit (partial misses). Multiple-return TLS can provide information about these partial hits so that a given beam can produce multiple echoes. Yin et al. (2020) tested several similar methods using the first or last echo per beam or averaging the first and last echoes for each beam. These approaches do not take full advantage of the information provided by multiple-return LiDAR and may lead to errors in estimating probability of transmission and leaf area density.

## 2.4. Equal-weighting method

To incorporate multiple-return LS information into the calculation of  $\overline{P}$ , one simple and easy to use method is to apply equal weighting of each echo within a given a pulse (e.g., Armston et al., 2013; Grau et al., 2017). The corresponding calculation of average probability of transmission is:

$$\overline{P}_{equal}^* = \frac{1}{B_{tot}} \sum_{k=1}^{B_{tot}} \frac{E_k^{after}}{E_k^{inside} + E_k^{after}},$$
(7)

where  $E_k^{after}$  and  $E_k^{inside}$  are the number of echoes (hit points) after the voxel and inside the voxel associated with the kth pulse, respectively. Eq. (7) incorporates multi-return TLS data into the estimation of transmission through a voxel without any additional information besides the hit coordinate. Each echo produced inside or after a given voxel for a given beam is weighted equally, and all beams are weighted equally.

An improvement to Eq. (7) proposed in the current work is to weight each beam by the fraction of echoes in a beam that that occurred after entering the voxel. Fig. 1 shows a simplified example of this with two beams that interact with a voxel. Each beam is represented by 200 rays and the number of rays intersecting each object is labeled. The probabilities of transmission based on individual beams shown are 0.667 (80/120) and 0.5 (100/200) for first and second beams, respectively. The mean of the results for each individual beam (i.e., the result of Eq. (7)) yields an overall probability of transmission of 0.583. This is different from the result when the probability is calculated based on all rays (entering the voxel) together (180/320 = 0.563). In the case of the first beam, which interacts with objects before reaching the voxel, the energy entering the voxel is reduced (i.e., 120/200 rays entering) compared with the second beam that hit nothing before entering the voxel (200/200 rays entering). The second beam in this example should, therefore, be weighted proportionally greater than the first beam in calculating the average probability of transmission through the voxel. Doing so reproduces the same overall probability calculated directly from all the rays together. This change yields a more

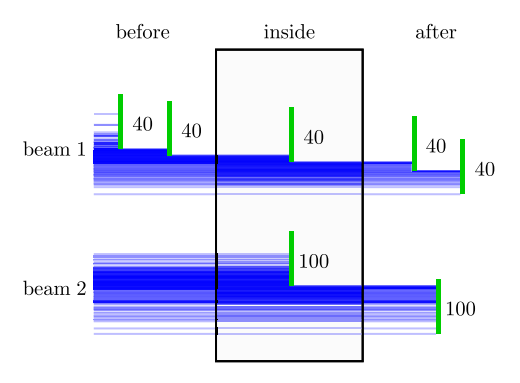


**Fig. 1.** Diagram illustrating the need to weight beams by fraction of energy entering the voxel. An example voxel (black outlined rectangle) is traversed by two beams from left to right, where individual rays within each beam are represented by blue lines. Individual leaves are shown as thick green lines and the associated echoes (hit points) are labeled with the number of rays intercepted. Each beam initially consists of 200 rays, but only a fraction of this energy enters the voxel for beam 1 due to intersections before reaching the voxel. Beam 1 has a transmission probability of 0.667 (80/120) and beam 2 has a transmission probability of 0.5 (100/200). Weighting the two beams equally results in a transmission probability estimate of 0.583, which is different from the estimate based on weighting the beams proportionally to the number of rays entering the voxel (0.563). See text for additional discussion. (For interpretation of the references to color in this figure legend, the reader is referred to the web version of this article.)

theoretically consistent transmission probability than  $\overline{P}_{equal}^{\ *}$  (Eq. (7)), is still relatively simple, and only uses information readily available from multi-return TLS point clouds:

$$\overline{P}_{equal} = \frac{\sum_{k=1}^{B_{tot}} \frac{E_k^{after}}{E_k^{inside} + E_k^{after}} \cdot BW_k^{equal}}{\sum_{k=1}^{B_{tot}} BW_k^{equal}}.$$
 (8)

## 2.5. Intensity-weighting method

Improvements in calculating the probability of transmission may be possible if the proportion of energy hitting the object associated with each echo can be estimated instead of assuming equal energy across all echoes within a given beam (Grau et al., 2017). Using simulated intensity values recorded by the virtual TLS scanner to weight echoes rather than weighting echoes equally, the beam transmission probability for "intensity-weighting" is

$$\overline{P}_{intensity} = \frac{\sum_{k=1}^{B_{tot}} \frac{I_k^{after}}{I_k^{inside} + I_k^{after}} \cdot BW_k^{intensity}}{\sum_{k=1}^{B_{tot}} BW_k^{intensity}},$$
(9)

where  $I_{after}^k$  and  $I_{inside}^k$  are the simulated intensities of the echoes from after the voxel and inside the voxel for the kth beam, respectively. Simulated intensities are calculated as:

$$I = R * cos(\psi) * \rho, \tag{10}$$

where R is the number of rays representing a given beam hitting an object,  $\psi$  is the angle between the beam direction and the normal of the object surface, and  $\rho$  is the reflectance factor of the object at the wavelength of the LiDAR scanner (referred to as reflectivity in the remainder of this article). Transmittance and multiple scattering of the LiDAR beam were assumed negligible and were not simulated, though both are incorporated in the radiation model plugin of Helios and could potentially be included in future LiDAR simulations in situations where they are more likely to have an impact (e.g., with larger beam footprints).

#### 2.6. Ideal intensity-weighting method

Intensities measured by actual LiDAR scanners are not direct measures of the fraction of emitted beam energy associated with each hit point, but rather a measure of how much of that energy was reflected back to the scanner. Distance between the hit point and the scanner, the reflectivity of the hit object in the wavelength of the scanner, and the angle of the hit object relative to the beam direction all contribute to differences between energy intercepted by an object and scattered energy measured by the scanner (Béland et al., 2011). The distance effect can easily be removed since the distance between the scanner and object is measured by the LiDAR itself. Reflectivity of the various objects in the scene (e.g., leaves, branches, the ground surface) is often not known, but may be measured using a spectroradiometer. Angles of object surfaces at the point of beam intersection are also usually not known. Although in some cases they may be estimated by fitting surfaces to adjacent hit points (e.g., Bailey and Mahaffee, 2017a), a unique surface normal estimation is usually not available for all hit points due to unsuccessful surface fitting. The method used to convert the energy detected by the scanner into intensity values of discrete hit-points can also impact resulting intensity values and vegetation parameters (Hancock et al., 2015a).

The ideal intensity-weighting method described here weights echoes directly by the fraction of simulated rays intercepting objects, which represents the fraction of beam energy intercepted rather than the fraction reflected back to the scanner as in the "intensity-weighting" method described in Section 2.5. This eliminates the impacts of reflectivity and surface angles and thus represents a best-case scenario for actual TLS measurements in which the beam energy hitting any given surface is known perfectly and corrected for. In the simulations for this work, the angle between the beam direction and object is the term driving differences between  $\overline{P}_{intensity}$  and  $\overline{P}_{ideal}$ . Transmission using this ideal intensity-weighting method is

$$\overline{P}_{ideal} = \frac{\sum_{k=1}^{B_{tot}} \frac{R_k^{after}}{R_k^{inside} + R_k^{after}} \cdot BW_k^{ideal}}{\sum_{k=1}^{B_{tot}} BW_k^{ideal}},$$
(11)

where  $R_k^{after}$  and  $R_k^{inside}$  are the number of rays in the kth beam that intersect objects after the voxel and inside the voxel, respectively.

## 2.7. Exact-weighting method

The "exact-weighting" method for calculating transmission in this paper is identical to the "ideal intensity-weighting method" except that it also accounts for partial misses:

$$\overline{P}_{exact} = \frac{\sum_{k=1}^{B_{tot}} \frac{R_k^{after} + R_k^{miss}}{R_k^{inside} + R_k^{after} + R_k^{miss}} \cdot BW_k^{exact}}{\sum_{k=1}^{B_{tot}} BW_k^{exact}},$$
(12)

where  $R_k^{miss}$  is the number of rays in the kth beam that hit nothing.  $\overline{P}_{ideal}$  will always equal or underestimate  $\overline{P}_{exact}$ , which is the best estimate of the mean probability of transmission possible since 100% of the energy of each beam is accounted for. This method is used for comparison in these simulations, but would be difficult to apply with actual LiDAR data since, in practice, information about partial misses is not generally known and is difficult to estimate.

Fig. 2 illustrates another example and the resulting probabilities of transmission estimated using Eqs. (6), (8), (9), and (12). For simplicity, each beam has the same zenith angle and the same energy entering the voxel so that only the transmission terms in the equations are relevant (e.g., the result using Eq. (8) is the same as the result using Eq. (7)). In this simple example, probabilities of transmission differ substantially across the four methods.

#### 2.8. Virtual homogeneous voxels

The first set of simulations run for this study was based on three isolated homogeneous volumes of leaves. Three 1 m3 voxels containing square 'leaves' with random spatial distribution were constructed (Fig. 3a). The widths of these leaves were set at 2, 4, and 8 cm in different simulations and the number of leaves varied so that voxels had leaf area density of approximately 0.1, 0.5, 1, and 2  $m^2$   $m^{-3}$ . Leaves were positioned randomly inside the voxels and leaf orientations were sampled from a spherical distribution. The center of the middle voxel was positioned at 2 m above the ground surface, which was represented by a 1000 m × 1000 m patch. The patch dimension was chosen to correspond to the maximum scanner range set for simulations in this study. Reflectivity was constant at a value of 1 for all leaves and the ground surface. Variation in reflectivity would introduce additional uncertainty to the intensity values reported in actual LiDAR measurements, but was kept constant here for simplicity. The simulated TLS instrument was positioned at a height of 2 m and at a horizontal distance of 6 m from the voxel centers. This positioning was chosen so that the virtual scanner was above the lower voxel and below the upper voxel: beams sent from the scanner would hit the ground surface after passing through the lower voxel (no partial misses possible). and would intersect nothing after passing through the upper voxel (partial misses possible). The middle voxel represented an intermediate situation in which partial misses were possible in part of the voxel. Ten randomly generated sets of leaves within the voxels were simulated for all combinations of LAD and leaf size, resulting in a total of 120 unique canopy configurations simulated.

#### 2.9. Virtual trees

Three separate cases were considered using virtual almond trees: one using only a single isolated tree (Fig. 3b), the second considering the same tree, but in the context of an orchard (Fig. 3c), and the third distributing the same leaves in each voxel of the isolated tree case uniformly across the voxel to eliminate sub-voxel-scale clumping (Fig. 3d). The isolated tree case was expected to have an increased probability of partial misses, whereas other trees outside the voxel in the orchard case were expected to intercept more rays and lead to less partial misses.

The orchard case was set up to represent a sub-section of an actual almond orchard block where physical LiDAR scans were previously collected. This block was 9 years old at the time of scanning and was located at Nickels Soil Laboratory near Arbuckle, California. Row spacing in the block was 6.096 m (20 ft) and the within-row tree spacing was  $4.572~\mathrm{m}$  (15 ft). The subsection that was scanned consisted of 11 trees in each of four adjacent rows planted with the Aldrich, Nonpareil, Sonora, and Independence varieties. Tree heights ranged from approximately  $4.9~\mathrm{to}~7.2~\mathrm{m}$ , with the main tree having a height of  $5.7~\mathrm{m}$ .

The branching structures of the isolated tree (one of the Nonpareil trees near the center of the block) and its eight immediate neighbors were reconstructed using leaf-off LiDAR scans. The collected point clouds were pre-processed manually to segment each individual tree and then reconstructions were performed using TreeQSM (Raumonen et al., 2013). Reconstructions consisted of adjacent cylinders that were then converted into Helios tube objects. Leaves were added for each tree on spurs that were inserted at a constant spacing on branching segments with radius less than 2 cm. This threshold was chosen to avoid spurs on the trunk and largest branches of the tree. The spacing between spurs was set by experimentation such that resulting total leaf area for the tree would exceed the highest LAI case of 4. Individual spurs were then randomly removed until the desired LAI for each case was achieved. Reconstructed branches were not included in simulations; they were deleted after using them to distribute the leaves. This was done to reduce computational expense of the simulations and to

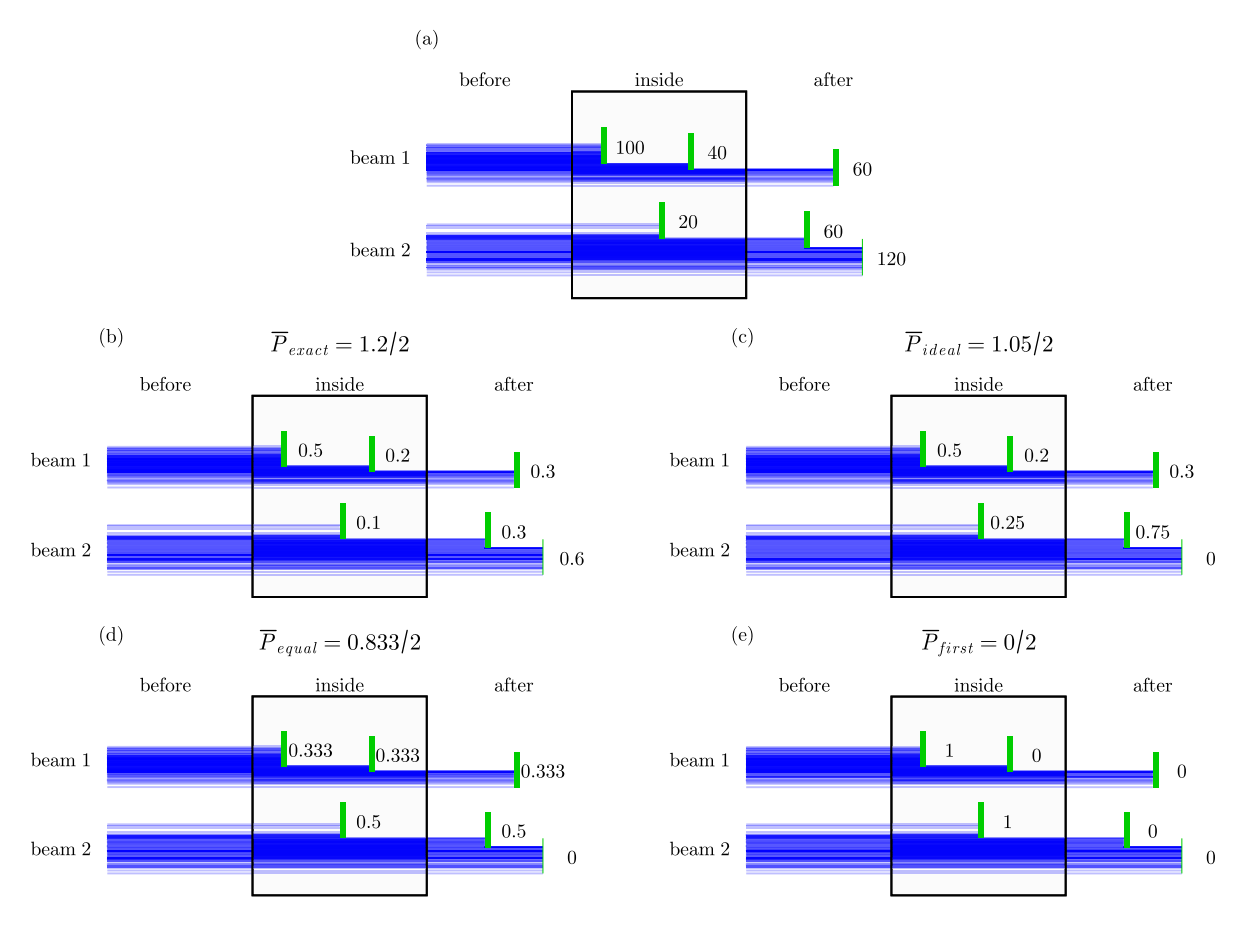


Fig. 2. Diagram illustrating differences between weighting approaches for an example voxel (black outlined rectangle) traversed by two beams from left to right, where individual rays within each beam are represented by blue lines. Each beam initially consists of 200 rays and all rays enter the voxel. Individual leaves are shown as thick green lines. (a) echoes (hit points) associated with a beam hitting each leaf are labeled with the number of rays intercepted. (b-e) Diagrams identical to (a) except echoes are labeled with the fraction of beam energy corresponding to (b)  $\overline{P}_{exact}$ , (c)  $\overline{P}_{ideal}$ , (d)  $\overline{P}_{equal}$ , and (e)  $\overline{P}_{first}$ . (For interpretation of the references to color in this figure legend, the reader is referred to the web version of this article.)

simplify the generation of the homogeneously distributed case. Leaves were given a realistic leaf shape using a PNG image as a transparency mask and individual leaf area was approximately 15.85 cm<sup>2</sup>. Leaves that intersected the faces of the voxel grid were sliced into triangles to ensure accurate reference leaf area for each voxel. Leaves outside the voxel grid were cropped out for the isolated tree case. In the distributed case, leaves within each voxel were randomly re-positioned within the voxel.

Separate reconstructions were performed to set the main tree LAI (one sided leaf surface area per unit ground area, where the ground area is the row spacing × tree spacing) to 1, 2.5, and 4.  $LAD_{ref}$  and  $\overline{G}_{ref}$  for individual voxels in these 3 cases are shown in Fig. 4.  $\overline{G}_{ref}$  tended to be close to 0.5 (matching a spherical angle distribution) except at very low values of  $LAD_{ref}$  where it varied greatly because there were not many leaves in those voxels. The LAI of each of the trees surrounding the main tree was kept at 2.5 for consistency.

Additional trees in the simulation were represented by a triangular mesh bounding envelope constructed using the alphashape3D R package (Lafarge and Pateiro-Lopez, 2020) and the TreeQSM cylinder nodes (red envelopes in Fig. 3). The triangular mesh had the same reflective properties as the leaves and ground: a reflectivity of 1 and transmissivity of 0. This was done to reduce the number of primitives represented in the simulations and reduce simulation time while still representing trees beyond the scanners that could generate hit points. In total, the orchard simulations represented 9 rows of 11 trees each. A 1000 m  $\times$  1000 m patch representing the ground was also included in all simulations. As with the isolated homogeneous voxel simulations, the reflectivity of all surfaces was set to constant value of one for simplicity.

In all cases a  $6 \times 5 \times 6$  voxel grid was horizontally centered on the trunk of the main tree, with horizontal dimensions matching the row and tree spacing and a vertical dimension of 6 m. This resulted in an overall voxel grid volume of 27.87 m<sup>3</sup> and individual voxel volumes of 0.929 m<sup>3</sup>. This voxel size was used for all analysis in this work unless otherwise noted and was near the 1 m<sup>3</sup> size found by Grau et al. (2017) to produce the most accurate LAD estimates compared with other smaller voxel sizes tested. Other studies have used somewhat smaller voxel sizes that may reduce the impact of vegetation clumping (e.g., Béland et al., 2011). Additional simulations were run with smaller voxels that had dimensions one-half and onefourth the length of the main voxels described above, referred to as "medium", "small", and "large" voxels, respectively. Virtual TLS scanners were positioned at four locations around the voxel grid where leaf-on LiDAR scans had previously been collected in the field. These positions were approximately 4.9 m from the main tree's trunk at a height of approximately 1.8 m. These simulations all used the reference beam size that matched the specifications of the VZ-1000 scanner.

## 3. Results

## 3.1. Isolated homogeneous voxels

Several basic expectations of the different methods were confirmed based on the isolated homogeneous voxel simulations. First,  $\overline{P}_{exact}$  was in close agreement with  $\overline{P}_{ref}$  (Fig. 5). This means that perfect beamweighting of TLS data (including accounting for partial misses) resulted in transmission probability that closely matched the expected reference

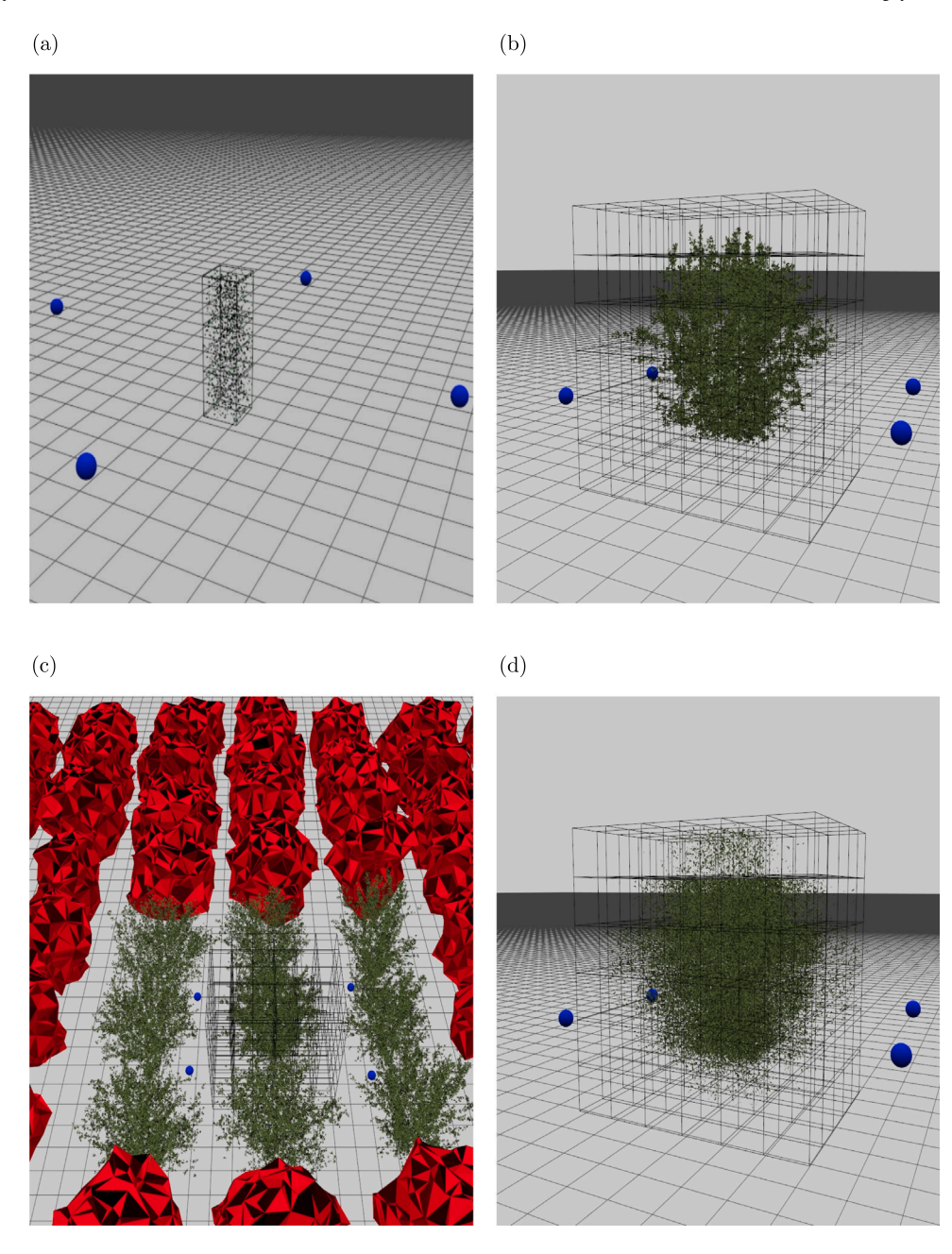


Fig. 3. Visualizations of example virtual canopy geometries used in this study. (a) isolated homogeneous voxels with  $LAD = 1 \text{ m}^2 \text{ m}^{-3}$  and leaf dimension = 4 cm, (b) isolated almond tree with LAI = 4, (c) overhead view of almond tree within an orchard, and (d) almond tree with leaf area distributed uniformly within each voxel (no sub-voxel-scale clumping). Blue spheres in all panels show the location of virtual TLS scanners.

value calculated using known LAD, known G, and Eq. (1) for these homogeneous isolated voxel cases, which suggests that the assumptions inherent in Beer's Law were generally satisfied and the number of beam samples was sufficient. Median and mean differences between  $\overline{P}_{exact}$  and  $\overline{P}_{ref}$  over these simulations were within 0.25% and all differences were within about 3.5% of the reference value. In terms of estimated LAD, mean and median differences between  $LAD_{exact}$  and  $LAD_{ref}$  were within about 0.5%, most differences were within 5%, and the maximum difference observed was about 12.5% (which occurred for very small leaf area density of  $LAD_{ref}=0.1$ ; Fig. 6). Some error can be expected in applying Eq. (1) to canopies that do not perfectly satisfy the assumptions of Beer's Law, primarily that radiation-intercepting elements are uniformly distributed and much smaller than the beam mean free path (Ponce de León and Bailey, 2019).

A second basic expectation that was confirmed was that  $\overline{P}_{ideal}$  closely agreed with  $\overline{P}_{exact}$  for the lower voxel case (Fig. 5). This was

expected because the only difference between the two methods is the inclusion of partial misses in  $\overline{P}_{exact}$ . Since all transmitted portions of beams intercepted the ground surface, there were no partial misses and thus the two methods should be identical.

The third basic expectation was that all methods that did not account for partial misses (i.e., all methods aside from  $\overline{P}_{exact}$ ) would perform identically for the upper voxel case. They indeed did perform identically and resulted in substantial underestimations of  $\overline{P}_{ref}$  and over-estimations of  $LAD_{ref}$  in the upper voxel case. They yielded identical underestimations of  $\overline{P}_{ref}$  because there were no surfaces to intercept beams behind the upper voxel in these simulations. In other words, any part of a beam that was transmitted through the voxel would be considered a partial miss and thus was not taken into account by these methods. Only beams that did not hit any surface within the voxel would be considered transmitted and thus transmission was underestimated substantially. Translated into terms of LAD, errors

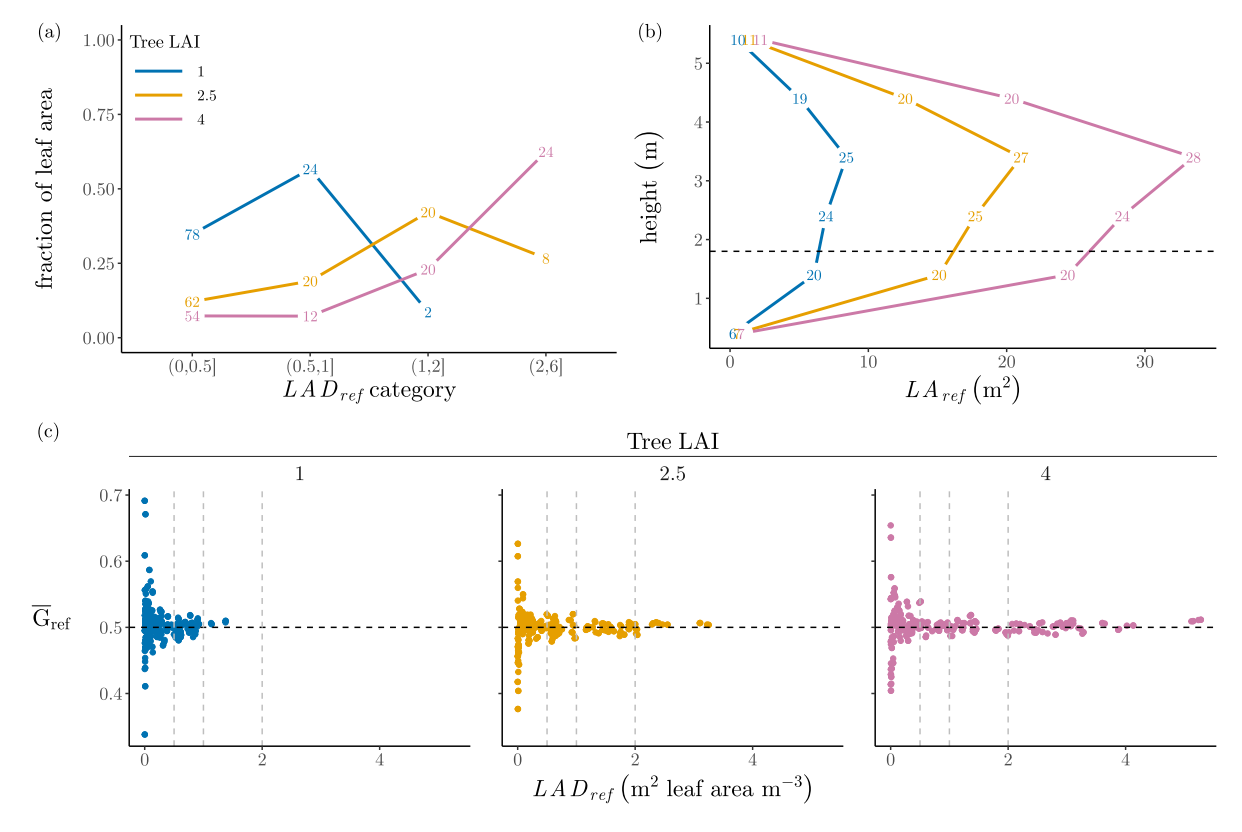


Fig. 4. Plots showing known properties of the virtual trees used in this work. (a) Fraction of tree leaf area in each  $LAD_{ref}$  category for the three simulations differing in tree LAI. The number of voxels falling into each category are indicated. (b) Total reference leaf area in each of the six vertical voxel layers. The number of voxels falling into each layer are indicated and the horizontal dashed line shows the average height of the virtual LiDAR scanners. (c)  $LAD_{ref}$  plotted against  $\overline{G}_{ref}$ . Individual points represent individual voxels. Cases with different tree LAI are shown in different panels horizontally. The horizontal dashed line shows  $\overline{G}_{ref} = 0.5$  and the vertical dashed lines show breaks between the  $LAD_{ref}$  categories shown in (a).

could be greater than 250% for the highest value of  $F_r$  (the ratio of the beam footprint diameter to the leaf dimension) tested. The greater magnitude percentage differences in LAD compared to percentage differences in P occur given the negative and exponential relationship between the two variables (i.e., Eq. (1)). This is especially noticeable at low values of  $LAD_{ref}$  (high  $\overline{P}_{ref}$ ) since even small differences are large relative to low values of  $LAD_{ref}$  (e.g., this leads to relatively similar percentage differences in LAD across the horizontal panels of Fig. 6, whereas the percentage differences in  $\overline{P}$  in Fig. 5 vary more across the panels). On a related note,  $\overline{P}_{first}$  performed similarly for all three voxels since it disregards partial hits after the voxel and thus only accounts for fully transmitted beams, regardless of if there is actually a surface after the voxel that intercepts the beams. Thus,  $\overline{P}_{first}$  had the greatest underestimates of  $\overline{P}_{ref}$  and overestimates of  $LAD_{ref}$  of all methods tested.

The last basic expectation was that errors should generally increase with  $LAD_{ref}$  and  $F_r$ . As  $LAD_{ref}$  increases and as the beam footprint increases in size relative to the dimension of leaves in the voxel, beams are more likely to hit more than one surface, whether multiple leaves within the voxel or ground after the voxel. This situation makes the choice of weighting approach more important. When beams are very small relative to objects in the voxel, they are most likely to hit entirely on a single object in the voxel or hit entirely on the ground after the voxel. In these cases the choice of weighting method has little impact and errors due to weighting method are reduced.

While higher errors were expected with larger values of  $LAD_{ref}$  and  $F_r$ , it is not immediately obvious why these errors bias towards underestimation of transmission and thus overestimation of LAD for all these methods. For  $\overline{P}_{first}$ , this bias is clear since for beams that hit partially inside and partially after a voxel, transmission is considered zero. For  $\overline{P}_{equal}$ ,  $\overline{P}_{intensity}$ , and  $\overline{P}_{ideal}$ , partial misses may explain part

of the transmission underestimate bias in the upper and middle voxels. However the bias persists for  $\overline{P}_{equal}$  and  $\overline{P}_{intensity}$  even in the lower voxel where no partial misses are possible.

For the equal-weighting approach, this means that beams tend to have a greater number of hit points inside the voxel compared with after the voxel as  $F_r$  increases. This makes sense because larger beams are more likely to hit multiple objects. In the voxel there are many potential objects that can generate multiple hit points. If there is only a flat ground surface after the voxel, the number of hit points will depend on the angle of the ground relative to the beam (how spread out the beam is over the surface) and the pulse distance threshold which determines how close multiple hit points can be to each other before they are merged. Given the  $T_{pd}$  value of 11 cm used in this study, a maximum of 12 hit points per beam could be generated assuming the beam direction corresponded to opposite corners of the 1 m<sup>2</sup> voxel and that parts of the beam hit leaves every 11 cm. On the other hand, a beam would need to be at a very oblique angle to the ground in order for that many hit points to be generated after the voxel. So for a beam that is half intercepted by leaves in the voxel and half intercepted by the ground, more hit points are likely to be generated by the leaves inside than the ground after, leading to an underestimation of transmission by the equal-weighting approach.

For the intensity-weighting approach, the negative bias in transmission in the lower voxel is due to greater returned intensities within the voxel compared with after the voxel. This occurred because of differences in the mean angle of the leaves inside the voxel and the ground surface relative to the beam direction. In these isolated homogeneous voxel cases, leaves in the voxel had a spherical angle distribution, while the ground had just one angle relative to a given beam. In the former case, the fraction of area projected in the scanner direction (i.e., the  $\cos(\psi)$  term in Eq. (10)) was always approximately

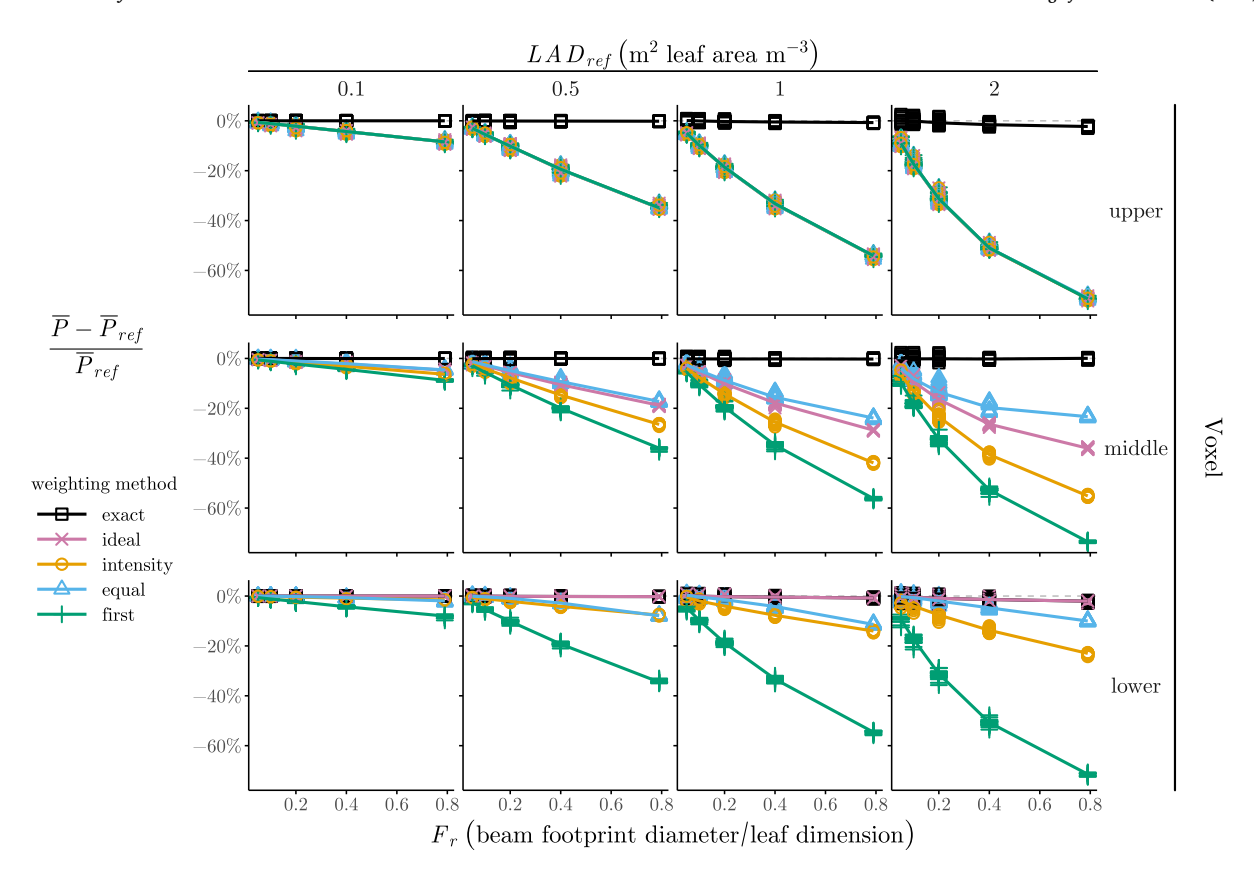


Fig. 5. Comparison of beam weighting methods for the isolated voxel simulations. Ratio of beam diameter at voxel center to leaf dimension ( $F_r$ ) is on the x-axis and error in estimated transmission probability,  $\overline{P}_r$ , between each method and the reference expressed as a percentage of the reference is on the y-axis. Simulations with varying nominal values of  $LAD_{ref}$  are shown as different panels horizontally and the results for the three voxel heights are shown in different panels vertically. Lines connect the median value corresponding to each simulation with the same  $F_r$  value. The horizontal dashed line indicates zero difference.

0.5, which corresponds to an angle of 60° between a beam and the ground. The fraction of ground area projected in the scanner direction for a set of beams traversing a voxel will vary depending on voxel size, scan pattern, scan position relative to the voxel, and the slope of the ground. For the lower voxel in this case, the ground was at an angle of approximately 79° relative to the beam directions, which corresponds to a fraction of ground area projected in the beam direction of approximately 0.19. This results in lower simulated intensities for ground hit points after the voxel compared with leaf hit points inside the voxel and an underestimation of  $\overline{P}_{ref}$  by  $\overline{P}_{intensity}$ . Scanner locations with beams more perpendicular to the ground surface (i.e.,  $\cos(\psi) > 0.5$ ) would be expected to result in overestimation of transmission in these cases. Additional simulations where the scanner position relative to the ground was varied confirmed this (not shown).

Although not used in this study, differences between the reflectivity of leaves and ground in the wavelength of the LiDAR scanner would also impact the accuracy of  $\overline{P}_{intensity}$ . If the ground was less reflective than the leaves, this would tend to lower  $\overline{P}_{intensity}$  compared with  $\overline{P}_{ideal}$ . If the ground was more reflective than the leaves,  $\overline{P}_{intensity}$  would tend to be higher than  $\overline{P}_{ideal}$  (all else being equal).

With these basic expectations verified, the remainder of this section focuses on differences between the idealized intensity-weighting  $(\overline{P}_{ideal})$ , non-idealized intensity-weighting  $(\overline{P}_{intensity})$ , and the equal-weighting  $(\overline{P}_{equal})$  approaches.

 $\overline{P}_{intensity}$  was lower than  $\overline{P}_{ideal}$  in the lower and middle voxels. In the lower voxel this corresponded to the bias towards higher intensities within the voxel compared with after the voxel on the ground which was due to a more oblique angle on average between the ground and the beams compared with between leaves and beams. In the middle voxel, half of the voxel is above the height of the scanner and half below. Beams traversing the upper half of the voxel encounter no

surfaces after the voxel and thus can produce partial misses, which causes an underestimation of  $\overline{P}_{exact}$  by both  $\overline{P}_{ideal}$  and  $\overline{P}_{intensity}$ . Beams transmitted through the lower half of the voxel are intercepted at an even more oblique angle by the ground than in the lower voxel, causing relatively lower intensities for echoes after the voxel than inside the voxel.  $\overline{P}_{intensity}$  thus underestimates  $\overline{P}_{exact}$  more than  $\overline{P}_{ideal}$ .

In the lower voxel,  $\overline{P}_{equal}$  is very close to  $\overline{P}_{intensity}$  in the lower  $LAD_{ref}$  simulations, but tended to have less error compared with  $\overline{P}_{intensity}$  as  $LAD_{ref}$  increased. There is a greater chance of the entire beam being intercepted within fewer hit points for more densely packed leaves. In other words, at a certain point, as  $LAD_{ref}$  is increased the beam is more likely to be fully intercepted by closely spaced leaves near the face of the voxel, rather than intercepted by multiple leaves spaced throughout the voxel that would generate multiple echoes. This tends to increase the transmission estimated by the equal-weighting approach, but does not impact the intensity-weighting approach.

In the middle voxel,  $\overline{P}_{equal}$  tended to be close to  $\overline{P}_{ideal}$ , with smaller errors. Improvements of  $\overline{P}_{equal}$  over  $\overline{P}_{ideal}$  increased as  $LAD_{ref}$  and  $F_r$  increased. It was initially hypothesized that  $\overline{P}_{equal}$  would always have higher errors than  $\overline{P}_{ideal}$  since the equal-weighting method is a simplified approximation of the latter, but this was not the case. This result indicates that for some beams, the fraction of echoes transmitted through the voxel was greater than the fraction of beam energy (rays) transmitted. This causes an overestimation of transmission by  $\overline{P}_{equal}$  that compensates for the underestimation caused by partial misses for both methods. On the other hand,  $\overline{P}_{ideal}$  will never overestimate transmission compared with  $\overline{P}_{exact}$ .

## 3.2. Virtual tree cases

Comparisons of  $\overline{P}$  values between the orchard, isolated tree, and distributed leaves cases indicated consistency in the design of these

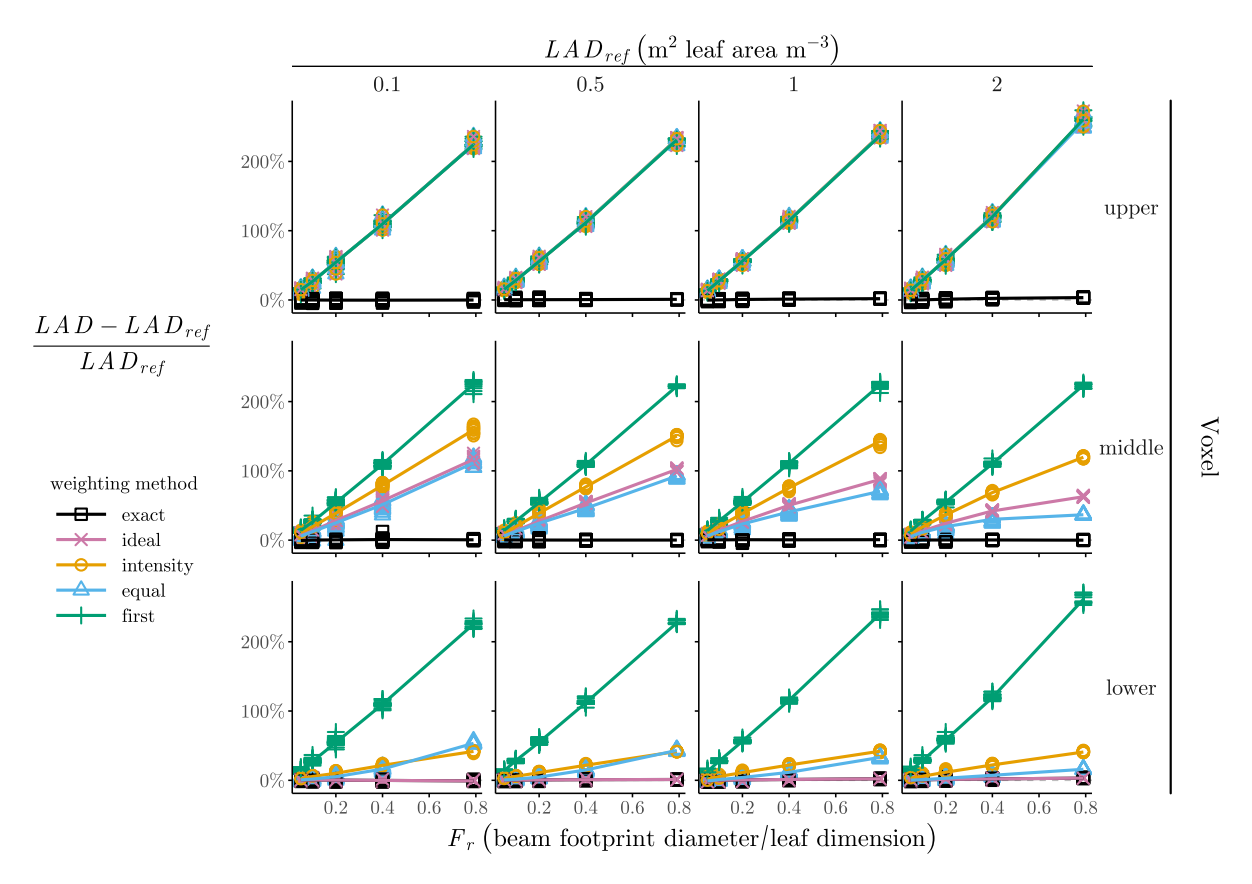


Fig. 6. Comparison of beam weighting methods for the isolated voxel simulations. Ratio of beam diameter at voxel center to leaf dimension ( $F_r$ ) is on the x-axis and error in estimated leaf area density,  $LAD_r$ , between each method and the reference expressed as a percentage of the reference is on the y-axis. Simulations with varying nominal values of  $LAD_{ref}$  are shown as different panels horizontally and the results for the three voxel heights are shown in different panels vertically. Lines connect the median value corresponding to each simulation with the same  $F_r$  value. The horizontal dashed line indicates zero difference.

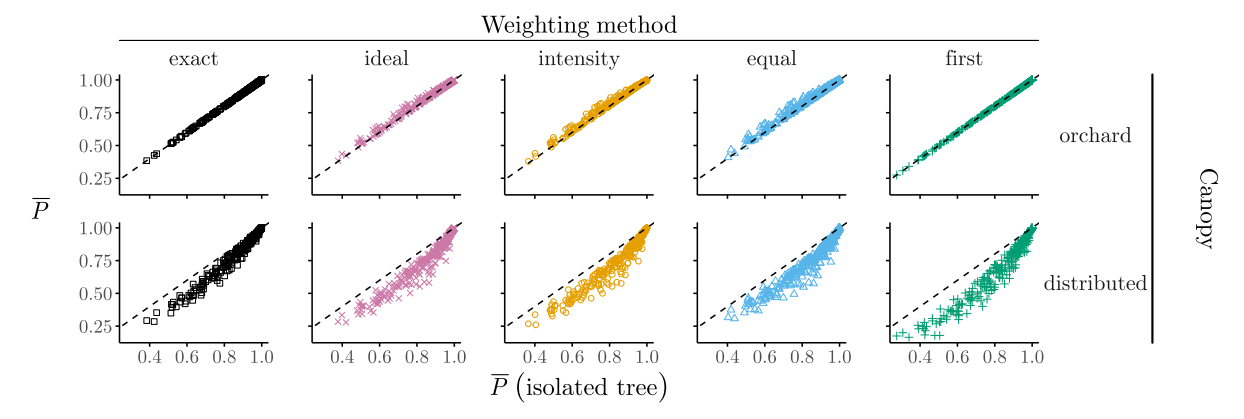


Fig. 7. Transmission  $(\overline{P})$  estimated for the isolated tree case plotted against  $\overline{P}$  for the orchard and distributed cases. The dashed black line is the 1:1 line. The different weighting methods are shown in different panels horizontally. Each point represents a single voxel and voxels for simulations with varying reference LAI are included in each panel.

cases.  $\overline{P}_{exact}$  and  $\overline{P}_{first}$  showed negligible differences between the isolated tree case and orchard case (Fig. 7), since neither were impacted by partial misses.  $\overline{P}_{ideal}$ ,  $\overline{P}_{intensity}$ , and  $\overline{P}_{equal}$  all tended to be higher for the orchard case than for the isolated tree case, since the additional surrounding trees reduced partial misses and therefore increased estimated transmission. All methods for estimating  $\overline{P}$  resulted in lower transmission estimates for the distributed leaves case compared with the isolated tree case (Fig. 7). This makes sense, since the sub-voxel scale clumping in the isolated tree case would tend to cause higher estimates of transmission compared with the case where leaves were distributed randomly within each voxel.

Comparisons of  $\overline{P}$  for each method against  $\overline{P}_{ref}$  are shown in Fig. 8.  $\overline{P}_{exact}$  tended to be greater than  $\overline{P}_{ref}$  in the orchard and isolated tree cases, and less than  $\overline{P}_{ref}$  in the distributed leaves case. The other methods overestimated  $\overline{P}_{ref}$  in some voxels and underestimated it in others for the orchard and isolated tree cases, and always underestimated  $\overline{P}_{ref}$  in the distributed leaves case.

The index of agreement between  $\overline{P}$  for all the beam-weighting methods and  $\overline{P}_{ref}$  was 96 to 99% for the isolated tree and orchard cases indicating good agreement (Fig. 9). NRMSE was 2 to 9% and mean bias was -0.018 to 0.052 for these cases. Agreement was lower for the distributed leaves case, with indices of agreement ranging 78 to 99%,

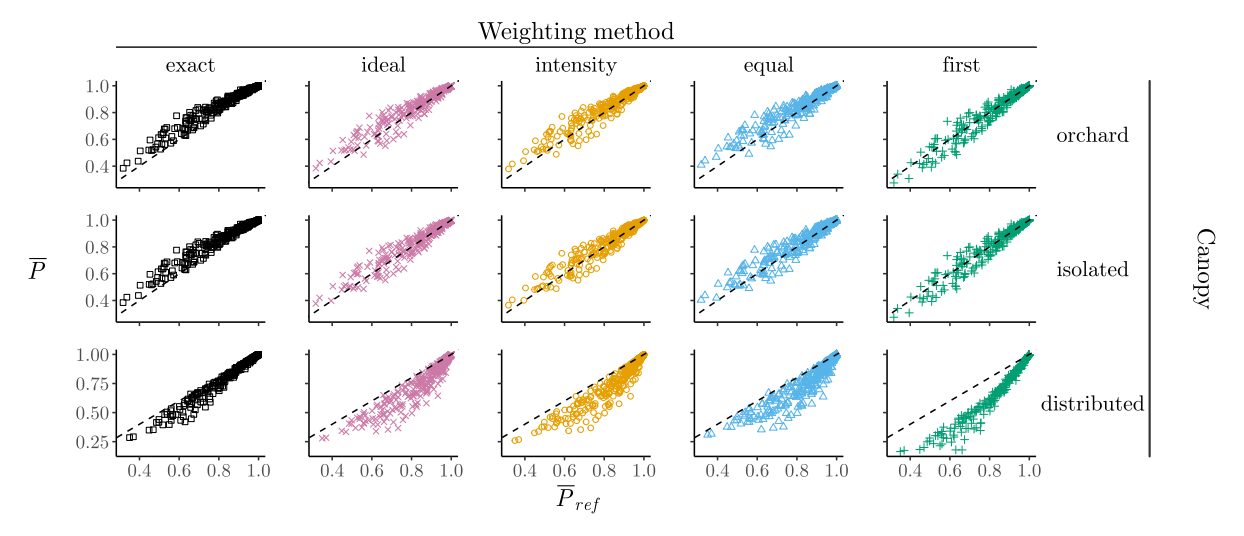


Fig. 8. Reference transmission  $(\overline{P}_{ref})$  plotted against  $\overline{P}$  for the different tree cases. The dashed black line is the 1:1 line. The different weighting methods are shown in different panels horizontally. The different canopy cases are shown in panels vertically. Each point represents a single voxel and voxels for simulations with varying reference LAI are included in each panel.

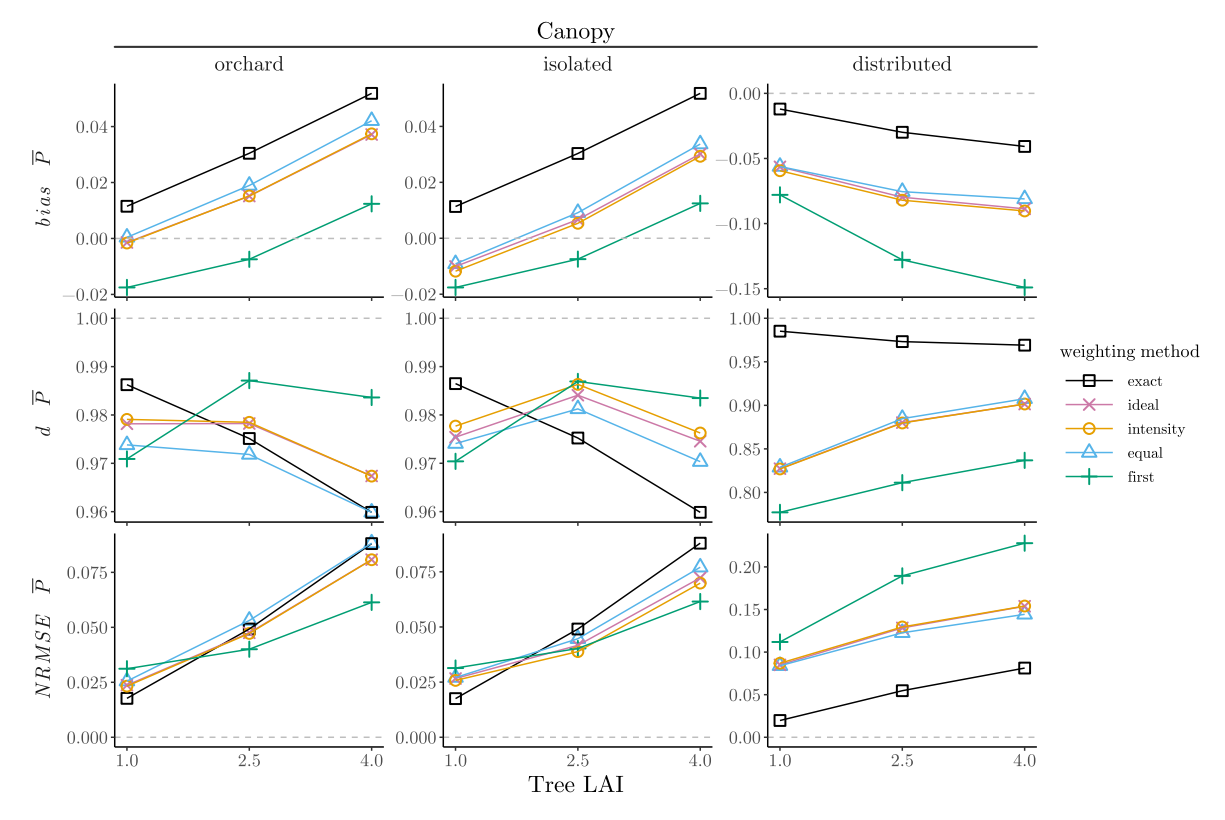


Fig. 9. Voxel level transmission statistics. Mean bias, index of agreement, and normalized root-mean-square error are shown in separate panels vertically. The different canopy cases are shown in separate panels horizontally. The y-axis scale is different for some panels to show more detail.

NRMSE ranging 2 to 23%, and mean bias ranging -0.149 to -0.012 (always negative).

In terms of LAD, the indices of agreement ranged 94 to 99%, NRMSE ranged 24 to 53%, and mean bias ranged -0.31 to 0.09  $\rm m^2\,m^{-3}$  for the isolated tree and orchard cases (Fig. 10). Again, agreement was lower for the distributed leaves case with indices of agreement ranging 56 to 98%, NRMSE ranging 34 to 358%, and mean biases ranging 0.059 to 2.14  $\rm m^2\,m^{-3}$ .

Given the importance of scanner height relative to voxel height on partial misses and performance of the different beam-weighting methods for the isolated homogeneous voxel cases, height impacts were also visualized for the tree cases (Fig. 11). The lowest and highest voxel levels had little leaf area (Fig. 4) and little bias in LAD. For the other vertical levels, biases tended to increase in magnitude with tree LAI. Bias of  $LAD_{exact}$  was negative for the orchard and isolated tree cases, and positive for the distributed case. This reflected the impact of leaf clumping in the orchard and isolated tree cases which increased estimated transmission and reduced estimated leaf area density compared to the distributed leaves case.

In all three canopy cases, biases in  $LAD_{ideal}$ ,  $LAD_{intensity}$ , and  $LAD_{equal}$  were closer to biases seen in  $LAD_{exact}$  for the lower levels. In the upper voxel levels these methods tended to be more positive

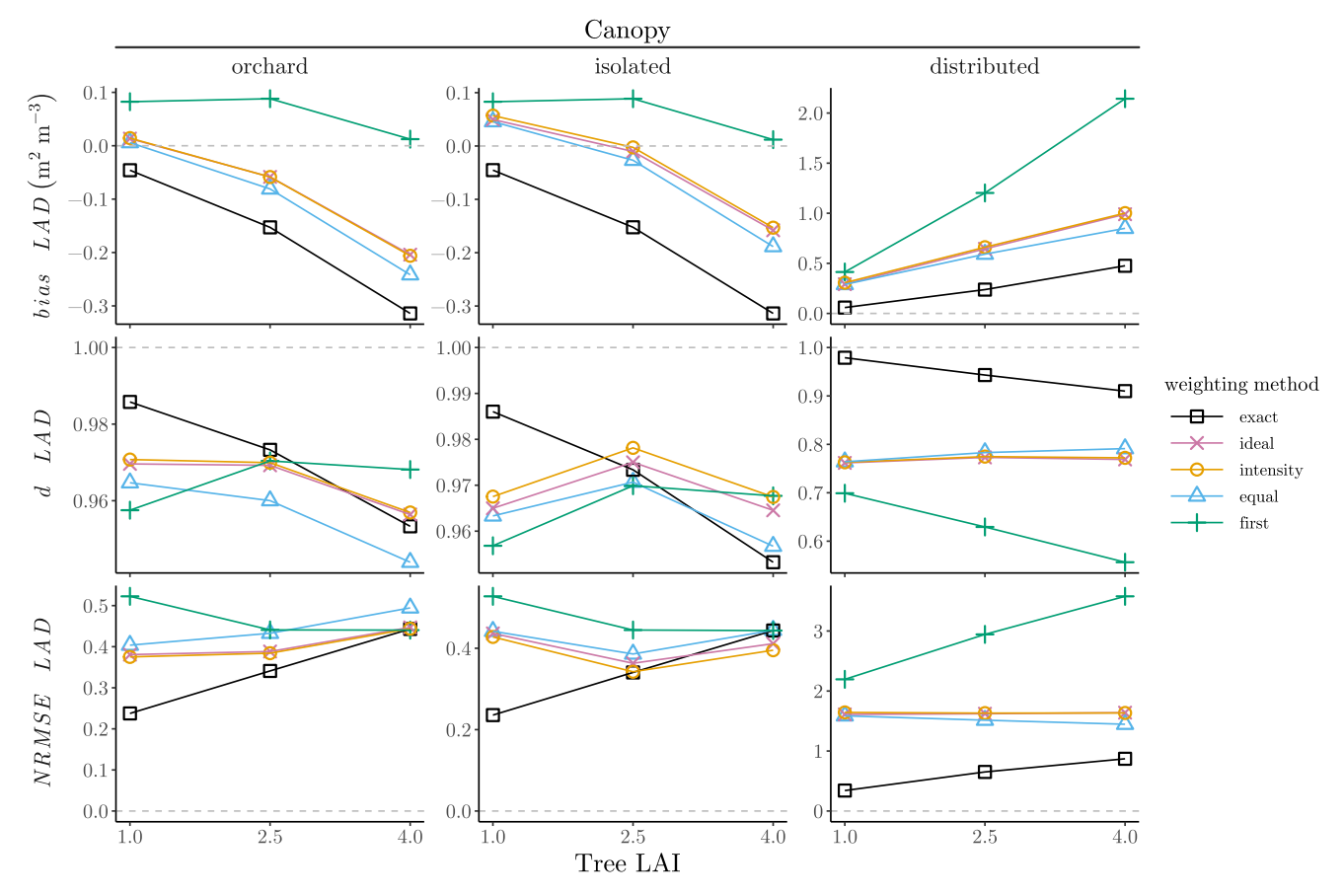


Fig. 10. Voxel level LAD statistics. Mean bias, index of agreement, and normalized root-mean-square error are shown in separate panels vertically. The different canopy cases are shown in separate panels horizontally. The y-axis scale is different for some panels to show more detail.

than at lower levels and overestimate  $LAD_{exact}$ . This was due to more partial misses at these levels which decreased transmission estimates and increased LAD estimates. Comparing the orchard and isolated tree cases, the impact of the surrounding trees in the orchard case was observed as more negative biases in the lower and middle levels, while there was little difference in bias at the higher levels. Biases in  $LAD_{ideal}$  and  $LAD_{imtensity}$  tended to be very similar, while  $LAD_{equal}$  tended to have slightly more negative bias at lower levels. At upper levels all three methods agreed closely.

Total LiDAR-estimated tree leaf area varied by canopy case, simulation tree LAI, weighting method, and voxel size (Fig. 12). The overall pattern of estimated total leaf area for the different weighting methods in relation to each other was similar across canopy cases and voxel sizes. The first-hits method always had the highest estimates, the exact-weighting method always had the lowest values, and the equal-weighting, intensity-weighting, and ideal intensity-weighting methods all had similar and intermediate leaf area estimates.

The orchard and isolated tree cases had a similar range of errors across methods. The first-hits method always overestimated reference leaf area by 1 to 62% for these two canopy cases. The exact beamweighting method tended to underestimate reference leaf area with differences ranging -29 to 3%. The equal-weighting, intensity-weighting, and ideal intensity-weighting methods all had similar intermediate estimates and could over- or underestimate reference leaf area depending on the tree LAI, canopy case, and voxel size. Differences between LAD estimated with these methods and  $LAD_{ref}$  ranged -22 to 24% and -17 to 42% for the orchard and isolated tree cases, respectively. The more positive differences for the isolated tree case were consistent with the impact of more partial misses and the more positive bias mid-canopy shown in Fig. 11. The equal-weighting method generally estimated about 1 to 7% lower total leaf area with respect to the reference area

than the ideal and intensity-weighting methods did for the isolated tree and orchard cases.

In the distributed leaves cases, all methods substantially overestimated total leaf area for all voxel sizes. The exact-weighting method had the lowest errors, but overestimated reference leaf area by 22 to 72%. This contrasts with the close agreement between  $LAD_{exact}$  and  $LAD_{ref}$  in the isolated homogeneous voxel cases (Fig. 6). These tree-level differences tended to be dominated by differences in the interior of the canopy where  $LAD_{ref}$  was also relatively high (not shown).

In the distributed leaves case, the first-hits method had the most error, overestimating reference leaf area by 149 to 266%. The other methods had intermediate errors overestimating reference leaf area by 80 to 109%, 93 to 121%, and 94 to 122% for the equal-weighting, ideal intensity-weighting, and intensity-weighting methods respectively. The equal-weighting method estimated leaf area about 0.7 to 17% lower with respect to the reference than the ideal and intensity-weighting methods. The higher estimated leaf area in the distributed leaves canopy case compared to the isolated tree and orchard cases was consistent with the expected impact of within-voxel clumping and known limitations of Beer's law when applied to clumped canopies (Ponce de León and Bailey, 2019; Bailey et al., 2020). In the isolated tree and orchard cases, the effect of leaf clumping on branches partially offset overestimation in leaf area due to the impact of partial misses. This offsetting effect was absent in the distributed leaves simulation.

Differences between leaf area estimates with each method and reference leaf area became more positive as voxel size was decreased (Fig. 13). Total leaf area estimates for the medium-sized voxels (i.e., with dimension near 0.5 m) were 2%–27% greater than those for the large voxels. Estimates for the small voxels (i.e., with dimension near 0.25 m) were 5 to 60% greater. In each case, estimated leaf area increased less with decreasing voxel size for the distributed canopy case

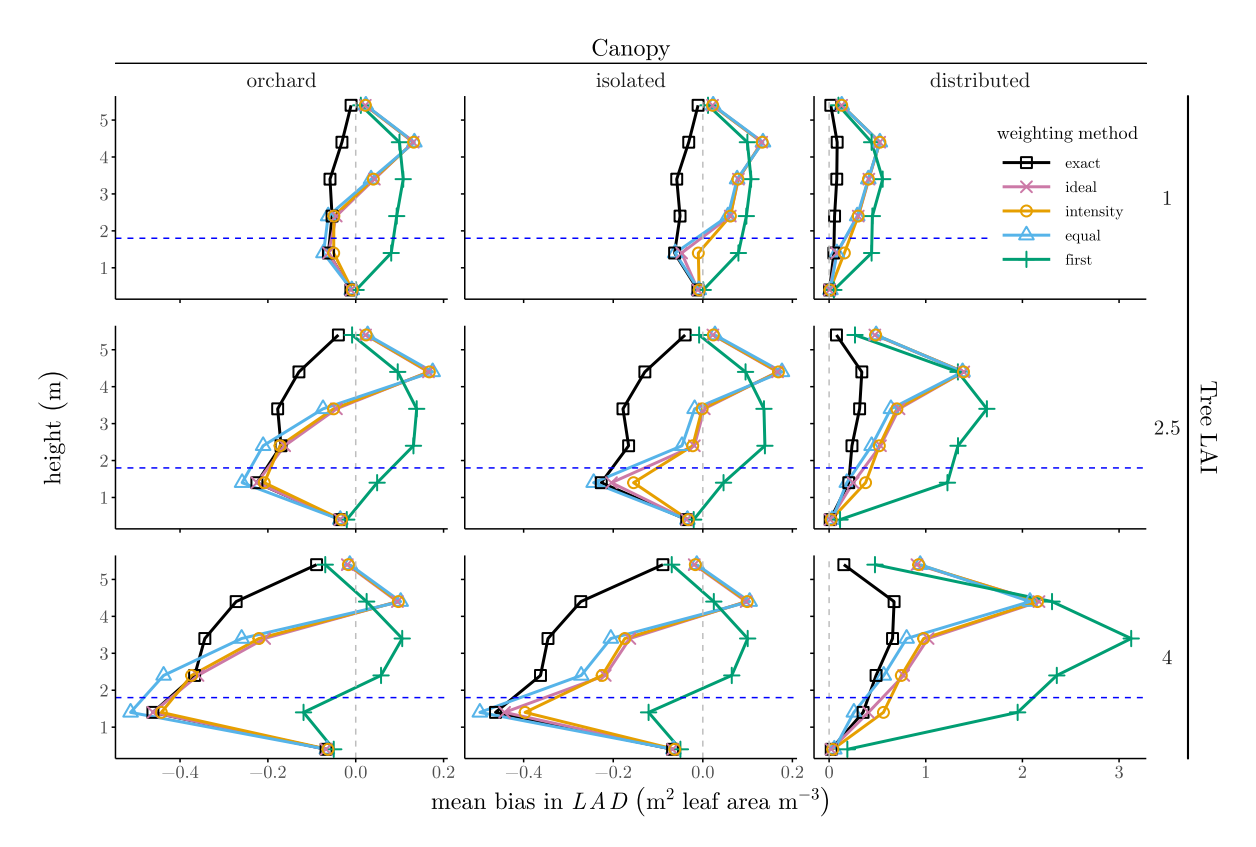


**Fig. 11.** Mean bias in *LAD* for different beam-weighting methods plotted against voxel height. The different canopy cases are shown in separate panels horizontally and the different tree LAI cases are shown in separate panels vertically. The dashed blue line indicates the mean height of the virtual LiDAR scanners. (For interpretation of the references to color in this figure legend, the reader is referred to the web version of this article.)

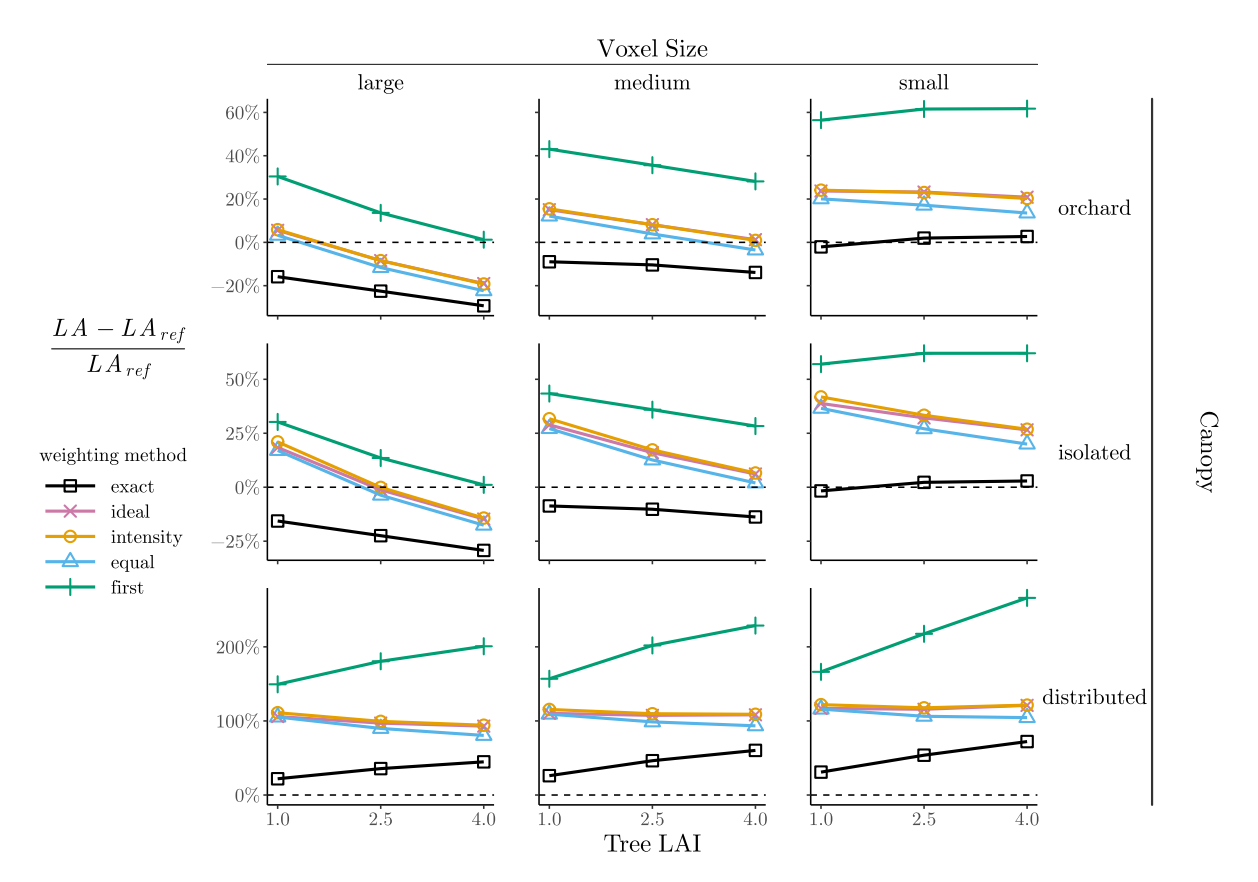
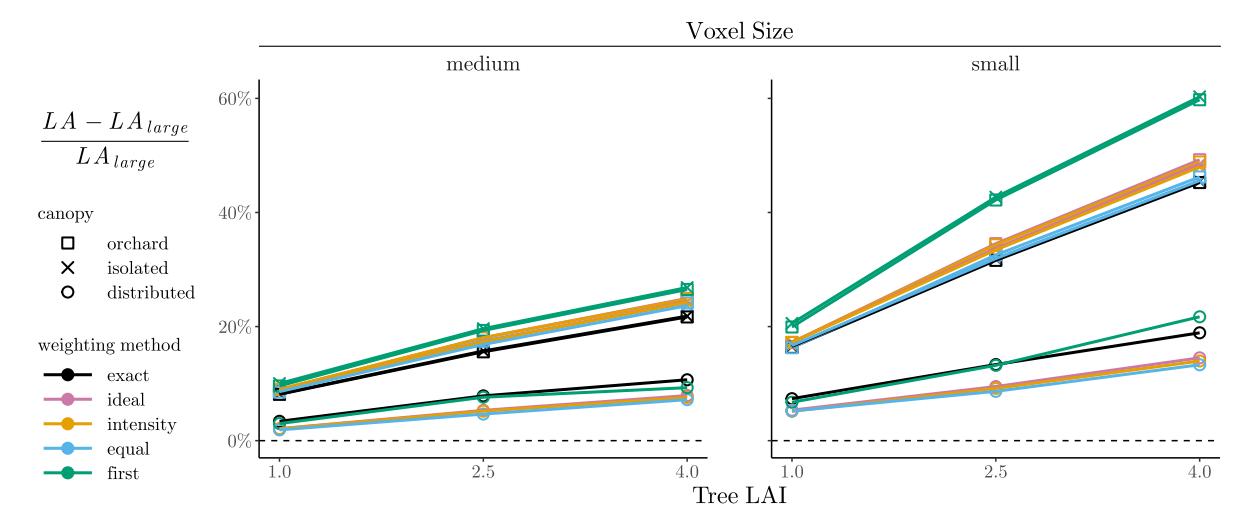


Fig. 12. Percentage difference between total tree leaf area estimated with synthetic LiDAR using different beam weighting methods and total known tree leaf area for each simulation ( $LA_{ref}$ ). Tree LAI of the simulation is on the x-axis. The orchard, isolated tree, and distributed voxel cases are shown in separate panels. Dashed horizontal lines indicate zero difference.



**Fig. 13.** Percentage difference between total tree leaf area estimated with synthetic LiDAR for the largest voxel size tested and for medium and small voxel sizes shown in separate panels. Tree LAI of the simulation is on the *x*-axis. The orchard, isolated tree, and distributed voxel cases are shown with different point shapes and different beam-weighting methods are shown with different colors. Dashed horizontal lines indicate zero difference. (For interpretation of the references to color in this figure legend, the reader is referred to the web version of this article.)

than it did for the isolated tree and orchard cases. This was expected given that smaller voxels have the tendency to reduce within-voxel clumping which was more prevalent in the isolated tree and orchard cases than in the distributed case. The change in leaf area with voxel size for the distributed canopy case may be indicative of clumping at the leaf level. As individual leaves get smaller, voxel leaf area would be less clumped and smaller differences in estimated leaf area with changes in voxel size would be expected.

#### 4. Discussion

Exact weighting of all energy in a beam was expected to yield the most accurate results since partial misses were accounted for, but this did not occur for most of the tree cases. Although there was very close agreement between  $LAD_{exact}$  and  $LAD_{ref}$  for the isolated homogeneous voxel cases, the tree cases, especially the distributed leaves tree case, exhibited substantially more error (Fig. 12). Such errors were somewhat surprising given that this case was similar to the isolated homogeneous voxel cases in that it was designed to more closely meet the assumptions of Beer's law (i.e., no clumping of leaves on branches).

The large differences observed between the isolated homogeneous voxel cases and distributed leaves tree cases point to the importance of factors other than weighting method and partial misses. First is the lack of sensitivity of transmission probability to changes in LAD as LAD increases, which is inherent due to the exponential relationship between these variables (Eq. (1)). Errors in  $LAD_{exact}$  tended to be greatest for denser canopies (Fig. 12), with the greatest errors tending to occur for high  $LAD_{ref}$  voxels towards the interior of the tree (not shown). As in the current study, Bailey and Ochoa (2018) also observed greater scatter in the relationship between simulated and reference leaf area for higher leaf area voxels, though they did not observe the same spatial pattern seen here.

This spatial pattern of increased errors in the tree interior points towards another likely contributor to the observed errors: occlusion. Although the minimum number of beams reaching any of the large voxels from the four scan positions was approximately 65,000, this was only about 12% of the maximum number of beams reaching any voxel. It is possible these dense, occluded interior voxels were not sampled adequately by the four scan positions, contributing to the errors in individual voxel LAD and the whole tree leaf area estimated.

Although the distributed leaves case was designed to exclude clumping of leaves on branches, the finite dimension of the leaves themselves

constitutes a type of clumping that may violate the assumptions of Beer's Law. Pimont et al. (2018) evaluated the impact of finite leaf size on estimations of leaf area density with Beer's Law and found up to  $\pm 50$ % confidence intervals when the projected area of an individual leaf was on the order of 10% the cross-sectional area of the voxel and the vegetation was dense. While the highest errors in the current study did tend to occur where leaf area was most dense, one-sided cross-sectional area of individual leaves were on the order of 0.19, 0.76, and 3.0% of the cross-sectional area of the smallest voxel face for the large, medium, and small voxels respectively. Thus the effects of finite leaf size in the current study are not likely to be as large as that observed by Pimont et al. (2018), but may be one contributor to the large biases in LAD observed

In all cases, differences between the equal-weighting and intensityweighting methods were relatively small, with the equal-weighting method generally estimating slightly higher transmission probabilities and slightly lower leaf area densities than the intensity based methods. The equal-weighting method was generally slightly closer to the exact beam-weighting method which perfectly accounted for all beam energy including partial misses. Thus, in cases where exact beam-weighting produced accurate P and LAD estimates, the equal-weighting method was expected to perform better than the intensity-weighting and even the idealized intensity-weighting methods. However, in the case of clumped canopies which did not match the basic assumptions of Beer's Law, the situation was not clear cut. Which method was more accurate was dependent on canopy characteristics including overall LAI and sub-voxel scale leaf clumping. For voxels with clumped leaves (i.e., the orchard and isolated tree cases in this study), the intensity based methods did tend to be slightly more accurate due to offsetting errors; transmission was generally underestimated in these cases due to clumping and intensity-weighting methods tended to have slightly higher transmission estimates, thus producing slightly more accurate results. Using smaller voxels helped reduce the impact of clumping and, in these cases, the intensity-based methods tended to have slightly more error than the equal-weighting method. Applying corrected intensitybased weighting based on the approaches considered in this work (i.e., the idealized intensity-weighting method) with actual TLS data may not be justified given the difficulty of determining the corrected fractional echo intensity from real TLS data, and the small improvement relative to other larger sources of error like clumping and occlusion. Applying the equal-weighting method to real TLS data is straightforward and is not expected to substantially change accuracy of LAD estimates.

Performance of the equal-weighting approach reported here was roughly similar to results reported by Grau et al. (2017) despite some differences in the canopy. They reported a relative bias in total plant area index (PAI) of 33% for an isolated tree with known PAI of 0.85, 1  $\rm m^3$  voxels, and a single scan position. The relative difference in total tree leaf area for the most comparable isolated tree simulation presented here was 17%, but for a shorter tree, a higher reference LAI (1), slightly smaller voxels, and four scan positions instead of one.

As far as we are aware, no other studies have compared multiple weighting methods including intensity-based weighting and equal weighting of multiple echoes within a beam in the context of terrestrial LiDAR data. Armston et al. (2013) and Yin et al. (2020) evaluated multiple methods, including those using intensity-based weighting, but for aerial LiDAR data in which the scanner was always above the canopy and the ground prevented partial misses. Armston et al. (2013) reported relatively small differences in gap probability between equal weighting and intensity weighting approaches. This is similar to the small differences between these methods generally found in the present study. In the case of voxels below the height of the scanners, where partial misses were not possible, results for the idealized intensityweighting method investigated here were generally consistent with those reported by Yin et al. (2020) for ALS simulations in the same LAI range; intensity-based methods estimated higher transmission than the equal-weighting method. The (non-idealized) intensity-weighting approach, on the other hand, often estimated lower transmission than the equal-weighting method in this study for voxels not impacted by partial misses. This could be due to the more oblique beam angles with respect to the ground for the TLS cases compared with more overhead scan positions in the ALS simulations. Beams more perpendicular to the ground are expected to estimate higher transmission compared with more oblique beams and compared with the idealized intensity-weighting approach.

This study found the first hits method differed most from the exact beam-weighting method, consistently underestimating transmission probability and overestimating LAD. For the high LAI, clumped canopies examined here this actually resulted in the most accurate total tree LAD estimate of any of the methods tested when using large voxels, since clumping caused underestimates by the other methods which were compensated by the relative overestimation using the firsthit method. The performance of this method also appeared to be independent of the fraction of partial misses, with a tendency towards underestimating transmission probability even when no partial misses were possible. Grau et al. (2017) and Yin et al. (2020) also found consistent underestimation of transmission using the first-hits data with TLS and ALS, respectively. Armston et al. (2013) found that using first returns also resulted in the most error in gap probability compared to their manual measurements, but, in contrast, reported overestimates of gap probability.

Results from the isolated homogeneous voxel cases (Section 3.1) showed increasing underestimates of transmission probability (overestimates of LAD) as the size of the beam approached the size of the leaf. This was due to an increase in partial misses. In the context of clumped canopies with smaller leaves (e.g., needle-leaf forests), the decrease in transmission (associated with an increase in partial misses) would be expected to counteract overestimates due to clumping even more than in the case of larger almond leaves simulated in this study. If all else was equal, this would lead to higher LAD estimates. Smaller leaves may also lead to more hit points and could impact the equal weighting method if the ratio of the number of hit points inside and after a voxel changes.

## 5. Conclusions

Probability of TLS beam energy transmission through voxels was calculated using a range of methods, including simplified approaches

used in previous work, intensity-based approaches, and idealized methods in which the fraction of intercepted beam energy associated with each echo is known. The latter are relatively straightforward to implement in synthetic LiDAR simulations and can produce a perfect intensity-based weighting while avoiding complications from actually attempting to calculate the energy intercepted in each echo from intensity information returned by actual TLS data. Such a correction of actual TLS data requires additional information that is not generally available from the TLS data itself (i.e., the angles and reflectivities of all scanned surfaces, and information about partial misses). The main question addressed in this research was whether corrected intensity-based weighting methods actually have the potential to improve transmission probability and leaf area density estimated using TLS data compared to simplified methods that are easier to implement with actual TLS data. Overall, it was concluded that the intensitybased methods tested did not offer a consistent advantage over the equal-weighting method for the cases examined in this work.

The impact of partial misses on transmission and LAD estimates was another question this article addressed. The synthetic LiDAR data simulation approach employed allowed for quantification of the impact of partial misses, which is otherwise difficult to estimate from actual TLS data. When partial misses were taken into account in the simulated TLS scans using the exact-weighting approach, voxel-level estimations of transmission could be substantially higher and estimates of LAD substantially lower than those produced with the idealized intensity-weighting method. This study also demonstrated that accurate transmission and LAD estimations are not assured even with exact weighting of echoes within each individual beam. The combined impacts of clumping, occlusion, and limitations of Beer's law at high LAD could have comparable or greater impacts on accuracy than differences between return-weighting approaches. Clumping and partial misses had offsetting effects on LAD, with clumping causing lower LAD estimates and partial misses causing higher LAD estimates. Overall accuracy of LAD estimates was dependent on the relative magnitude of these opposing effects and varied with canopy LAI, voxel size, and degree of sub-voxel scale leaf clumping.

Given the multiple sources of error observed in this study that combine to impact estimated *LAD*, future work is needed to separate their contributions and individually understand their dependencies. This could include exploring scanner configurations to best sample dense canopies, or even alternative/hybrid approaches to using Beer's Law for canopy LAD estimation in these situations. Empirical approaches to deriving relationships between LiDAR intensity and canopy cover fraction (e.g., Schraik et al., 2021; Korpela et al., 2013; Armston et al., 2013) could also be further explored.

## CRediT authorship contribution statement

**Eric R. Kent:** Writing – review & editing, Writing – original draft, Visualization, Validation, Software, Methodology, Investigation, Formal analysis, Conceptualization. **Brian N. Bailey:** Writing – review & editing, Validation, Software, Resources, Project administration, Methodology, Funding acquisition, Conceptualization.

## **Declaration of competing interest**

The authors declare the following financial interests/personal relationships which may be considered as potential competing interests: Eric R. Kent reports financial support was provided by Almond Board of California. Brian Bailey reports financial support was provided by US Department of Agriculture. Brian Bailey reports financial support was provided by National Science Foundation.

#### Data availability

Data will be made available on request.

# E.R. Kent and B.N. Bailey Acknowledgments

We thank Franz Niederholzer for providing information about and facilitating access to Nickels Soil Laboratory where some of the LiDAR data used to construct virtual trees in this study were collected.

We thank the anonymous reviewers that provided feedback and helped improve this article.

We acknowledge support from Almond Board of California grants PREC1 and HORT45, the USDA National Institute of Food and Agriculture Hatch project 1013396, and U.S. National Science Foundation grant IOS 2047628.

#### References

- Anderson, K., Hancock, S., Disney, M., Gaston, K.J., 2016. Is waveform worth it? A comparison of LiDAR approaches for vegetation and landscape characterization. Remote Sens. Ecol. Conserv. 2, 5–15.
- Armston, J., Disney, M., Lewis, P., Scarth, P., Phinn, S., Lucas, R., Bunting, P., Goodwin, N., 2013. Direct retrieval of canopy gap probability using airborne waveform lidar. Remote Sens. Environ. 134, 24–38.
- Bailey, B.N., 2019. Helios: a scalable 3D plant and environmental biophysical modelling framework. Front. Plant Sci. 10, 1185.
- Bailey, B.N., Mahaffee, W.F., 2017a. Rapid measurement of the three dimensional distribution of leaf orientation and the leaf angle probability density function using terrestrial LiDAR scanning. Remote Sens. Environ. 194, 63–76.
- Bailey, B.N., Mahaffee, W.F., 2017b. Rapid, high-resolution measurement of leaf area and leaf orientation using terrestrial LiDAR scanning data. Meas. Sci. Technol. 28, 064006
- Bailey, B.N., Ochoa, M.H., 2018. Semi-direct tree reconstruction using terrestrial LiDAR point cloud data. Remote Sens. Environ. 208, 133–144.
- Bailey, B.N., Ponce de León, M.A., Krayenhoff, E.S., 2020. One-dimensional models of radiation transfer in heterogeneous canopies: A review, re-evaluation, and improved model. Geosci. Model Dev. 13, 4789–4808.
- Béland, M., Baldocchi, D.D., Widlowski, J.-L., Fournier, R.A., Verstraete, M.M., 2014.
  On seeing the wood from the leaves and the role of voxel size in determining leaf area distribution of forests with terrestrial LiDAR. Agric. For. Meteorol. 184, 82–97.
- Béland, M., Widlowski, J.-L., Fournier, R.A., Côté, J.-F., Verstraete, M.M., 2011. Estimating leaf area distribution in savanna trees from terrestrial LiDAR measurements. Agric. For. Meteorol. 151, 1252–1266.
- Danson, F.M., Hetherington, D., Morsdorf, F., Koetz, B., Allgower, B., 2007. Forest canopy gap fraction from terrestrial laser scanning. IEEE Geosci. Remote Sens. Lett. 4, 157–160.
- Disney, M.I., Kalogirou, V., Lewis, P., Prieto-Blanco, A., Hancock, S., Pfeifer, M., 2010. Simulating the impact of discrete-return lidar system and survey characteristics over young conifer and broadleaf forests. Remote Sens. Environ. 114, 1546–1560.
- Grau, E., Durrieu, S., Fournier, R., Gastellu-Etchegorry, J.-P., Yin, T., 2017. Estimation of 3D vegetation density with Terrestrial Laser Scanning data using voxels. A sensitivity analysis of influencing parameters. Remote Sens. Environ. 191, 373–388.
- Halubok, M., Kochanski, A.K., Stoll, R., Bailey, B.N., 2022. Errors in the estimation of leaf area density from aerial LiDAR data: Influence of statistical sampling and heterogeneity. IEEE Trans. Geosci. Remote Sens. 60, 1–14.
- Hancock, S., Anderson, K., Disney, M., Gaston, K.J., 2017. Measurement of fine-spatial-resolution 3D vegetation structure with airborne waveform lidar: Calibration and validation with voxelised terrestrial lidar. Remote Sens. Environ. 188, 37–50.
- Hancock, S., Armston, J., Hofton, M., Sun, X., Tang, H., Duncanson, L.I., Kellner, J.R., Dubayah, R., 2019. The GEDI simulator: A large-footprint waveform lidar simulator for calibration and validation of spaceborne missions. Earth Space Sci. 6 (2), 294–310
- Hancock, S., Armston, J., Li, Z., Gaulton, R., Lewis, P., Disney, M., Danson, F.M., Strahler, A., Schaaf, C., Anderson, K., Gaston, K.J., 2015a. Waveform lidar over vegetation: An evaluation of inversion methods for estimating return energy. Remote Sens. Environ. 164, 208–224.

- Hancock, S., Essery, R., Reid, T., Carle, J., Baxter, R., Rutter, N., Huntley, B., 2015b. Characterising forest gap fraction with terrestrial lidar and photography: An examination of relative limitations. Agric. For. Meteorol. 189–190, 105–114.
- Heiskanen, J., Korhonen, L., Hietanen, J., Pellikka, P.K., 2015. Use of airborne lidar for estimating canopy gap fraction and leaf area index of tropical montane forests. Int. J. Remote Sens. 36 (10), 2569–2583.
- Hopkinson, C., Chasmer, L.E., 2007. Modelling canopy gap fraction from lidar intensity. In: ISPRS Workshop on Laser Scanning 2007 and SilviLaser 2007. IAPRS, Espoo, Finland, pp. 190–194.
- Hosoi, F., Omasa, K., 2006. Voxel-based 3D modeling of individual trees for estimating leaf area density using high-resolution portable scanning LiDAR. IEEE Trans. Geosci. Remote Sens. 40, 3610–3618.
- Itakura, K., Hosoi, F., 2019. Estimation of leaf inclination angle in three-dimensional plant images obtained from LiDAR. Remote Sens. 11 (3), 344.
- Jupp, D.L., Culvenor, D.S., Lovell, J.L., Newnham, G.J., Strahler, A.H., Woodcock, C.E., 2009. Estimating forest LAI profiles and structural parameters using a ground-based laser called 'Echidna®'. Tree Physiol. 29 (2), 171–181.
- Korpela, I., Hovi, A., Korhonen, L., 2013. Backscattering of individual LiDAR pulses from forest canopies explained by photogrammetrically derived vegetation structure. ISPRS J. Photogramm. Remote Sens. 83, 81–93.
- Lafarge, T., Pateiro-Lopez, B., 2020. alphashape3d: Implementation of the 3D alphashape for the reconstruction of 3D sets from a point cloud. R package version 1.3.1. https://CRAN.R-project.org/package=alphashape3d.
- Lu, L.X., Shuttleworth, W.J., 2002. Incorporating NDVI-derived LAI into the climate version of RAMS and its impact on regional climate. J. Hydrometeorol. 3, 347–362.
- Perez, R.P.A., Vezy, R., Brancheriau, L., Boudon, F., Grand, F., Ramel, M., Artanto Raharjo, D., Caliman, J.-P., Dauzat, 2022. When architectural plasticity fails to counter the light competition imposed by planting design: an in silico approach using a functional–structural model of oil palm. In Silico Plants 2022, diac009. http://dx.doi.org/10.1093/insilicoplants/diac009.
- Pimont, F., Allard, D., Soma, M., Dupuy, J.-L., 2018. Estimators and confidence intervals for plant area density at voxel scale with T-LiDAR. Remote Sens. Environ. 215, 343–370
- Pimont, F., Dupuy, J.-L., Rigolot, E., Prat, V., Piboule, A., 2015. Estimating leaf bulk density distribution in a tree canopy using terrestrial LiDAR and a straightforward calibration procedure. Remote Sens. 7995–8018.
- Ponce de León, M.A., Bailey, B.N., 2019. Evaluating the use of Beer's law for estimating light interception in canopy architectures with varying heterogeneity and anisotropy. Ecol. Model. 406, 133–143.
- Radtke, P.J., Bolstad, P.V., 2001. Laser point-quadrat sampling for estimating foliage-height profiles in broad-leaved forests. Can. J. Forest Res. 31, 410–418.
- Ramirez, F.A., Armitage, R.P., Danson, F.M., 2013. Testing the application of terrestrial laser scanning to measure forest canopy gap fraction. Remote Sens. 5, 3037–3056.
- Raumonen, Pasi, Kaasalainen, Mikko, Åkerblom, Markku, Kaasalainen, Sanna, Kaartinen, Harri, Vastaranta, Mikko, Holopainen, Markus, Disney, Mathias, Lewis, Philip, 2013. Fast automatic precision tree models from terrestrial laser scanner data. Remote Sens. 10, 491–520.
- Riano, D., Valladares, F., Condes, S., Chuvieco, E., 2004. Estimation of leaf area index and covered ground from airborne laser scanner (Lidar) in two contrasting forests. Agric. For. Meteorol. 124, 269–275.
- Schraik, D., Hovi, A., Rautiainen, M., 2021. Estimating cover fraction from TLS return intensity in coniferous and broadleaved tree shoots. Silva Fenn. 55 (4), http://dx.doi.org/10.14214/sf.10533.
- Sievänen, R., Raumonen, P., Perttunen, J., Nikinmaa, E., Kaitaniemi, P., 2018. A study of crown development mechanisms using a shoot-based tree model and segmented terrestrial laser scanning data. Ann. Botany 122, 423–434.
- Soma, M., Pimont, F., Durrieu, S., Dupuy, J.-L., 2018. Enhanced measurements of leaf area density with T-LiDAR: Evaluating and calibrating the effects of vegetation heterogeneity and scanner properties. Remote Sens. 10, 1580. http://dx.doi.org/ 10.3390/rs10101580.
- Yin, T., Qi, J., Cook, B.D., Morton, D.C., Wei, W., Gastellu-Etchegorry, J.-P., 2020. Modeling small-footprint airborne lidar-derived estimates of gap probability and leaf area index. Remote Sens. 12.
- Yuan, H., Dai, Y., Xiao, Z., Ji, D., Shangguan, W., 2011. Reprocessing the MODIS Leaf Area Index products for land surface and climate modelling. Remote Sens. Environ. 115, 1171–1187.